

## **Chapter 2.**

# **Convective-Stratiform Separation of Radar Reflectivity Fields for Real-Time Correction of Range-Dependent Biases in Radar Rainfall Estimates due to Vertically Nonuniform Profile of Reflectivity**

### **1. Introduction**

It is well known that vertically nonuniform profile of reflectivity is one of the biggest sources of error in quantitative precipitation estimation (QPE) using radar (Smith et al. 1991, Seo et al. 2000). In a nutshell, the vertical profile of reflectivity (VPR) effects are a height-to-range translation, according to the sampling geometry of the radar, of the reflectivity morphology of the precipitating cloud into range-dependent biases in radar QPE. Because radar reflectivity of hydrometeors depends very strongly on their phase, i.e., frozen, melting or liquid, the VPR effects figure prominently in radar estimation of stratiform precipitation. In convective precipitation, on the other hand, VPR is relatively vertically uniform and hence is not, in general, a significant source of error. To mitigate the VPR effects, the National Weather Service Hydrology Laboratory (NWS/HL) has developed the Range-dependent bias Correction Algorithm (RCA, Seo et al. 2000). In short, RCA estimates the mean VPR over the precipitating area in the entire scanning domain of the radar, and estimates multiplicative correction factors applicable to the raw radar reflectivity data as a function of range and elevation angle. While estimating mean VPR over the entire radar umbrella is less susceptible to sampling errors and computationally much less expensive than estimating local mean VPR, correction based on umbrella-wide mean VPR can produce unintended consequences in areas of embedded convection as explained below. Given that, in situations of mixed precipitation, stratiform precipitation occurs generally over a larger area than convective precipitation, it is likely that the umbrella-wide mean VPR is representative more of the stratiform precipitation than the convective. Correction of range-dependent biases based on such a mean VPR would generally reduce raw reflectivity at the ranges where the radar beam intercepts the freezing level and increase raw reflectivity beyond the above ranges where the radar beam samples ice particles. Accordingly, applying correction factors based on stratiform VPR in areas of convective precipitation would produce unrealistically large or small precipitation estimates depending on the height of the freezing level. For this reason, separating convective precipitation from stratiform, so that mean VPR may be sampled from and bias correction may be applied to the areas of stratiform precipitation only, has been recognized as a necessary first step before RCA. The purpose of this work is to develop an automatic algorithm for convective-stratiform separation based on volume scan radar reflectivity data, referred to herein as the Convective-Stratiform Separation Algorithm (CSSA), in support of RCA. The CSSA-RCA tandem

described above represents a ‘stratify-and-adjust’ strategy of first separating convective and stratiform areas of precipitation, and then estimating mean VPR and correcting range-dependent biases in the stratiform areas only. The net effect sought by the approach is equivalent to estimating local mean VPR and applying local correction of range-dependent bias. It is noted that such local estimation and correction is computationally too expensive to be operationally viable in the current WSR-88D environment.

Though we use the terms “convective” and “stratiform” rather freely throughout this paper, we are not necessarily interested in convective-stratiform separation in the storm-dynamical sense. Rather, our interest is primarily reflectivity-morphological, with the objective of separating instantaneous VPRs at all individual azimuth and range (hereafter abbreviated as “azran”) bins in the precipitating area into convective and stratiform groups such that VPR correction specific to precipitation type yields the biggest improvement in radar estimation of surface precipitation. It must also be noted that, in addition to supporting VPR correction, convective-stratiform separation may also be used to apply precipitation type-specific Z-R relationships. This microphysical aspect of convective-stratiform separation, however, cannot be effectively dealt with without first resolving the VPR effects, and hence is not considered in this work.

This chapter is organized as follows. In Section 2, we describe how the separation attributes, i.e. the physical and statistical attributes of local reflectivity morphology that possess skill in convective-stratiform separation, are selected. In Section 3, we describe how the separation attributes are used to estimate the conditional probability of the precipitation at some bin being convective. Section 4 describes how the separation procedure is evaluated. Section 5 provides conclusions and future research recommendations.

## **2. Identification of Separation Attributes**

Any procedure that attempts at convective-stratiform separation may be made an analogy with linear regression in which the predictand is the probability that the particular bin is in the convective (or stratiform) area and the predictors are a set of reflectivity-morphological attributes that possess significant skill in separating convective areas from stratiform. Herein, we refer to such attributes as ‘separation attributes.’ In identifying separation attributes, we assume that only the volume-scan reflectivity data are available. It is acknowledged that the height of the freezing level may also be available from sounding, surface observations or model output, which may be used to guide estimation of bright band height from the volume-scan reflectivity data. As may be seen in Fulton et al. (2001), however, it is difficult to make an objective use of the resulting information in an azran bin-specific manner. For this reason, we do not require that the freezing level be known from an external source.

To arrive at a set of skillful separation attributes, we tested a large number of physical and statistical attributes obtainable from volume-scan reflectivity data. For a complete list, the reader is referred to Fulton et al. (2001). The attributes were selected from the following process: 1) consider a candidate attribute, 2) estimate the attribute for each azran bin from the volume scan reflectivity data, 3) apply a threshold on the attribute field to render into a binary mask of convective and stratiform areas, 4) intersect the new binary map with all other such maps derived from other attributes, 5) visually assess whether the additional masking in Step 4 improves

convective-stratiform separation, 6) if it does, retain the attribute: if not, reject, 7) repeat Steps 1 through 6 until all skillful attributes are identified. For further details with graphical examples, the reader is referred to Fulton et al. (2001).

From the above process, we identified the following four separation attributes; 1) the maximum reflectivity in the vertical,  $r_x$  (dBZ), 2) the (minimum) local spatial correlation of  $r_x$ ,  $\min\{\rho_{rx}^a(1), \rho_{rx}^r(1)\}$ , 3) the (minimum) local spatial correlation of the height of the apparent convective core,  $\min\{\rho_{ht}^a(1), \rho_{ht}^r(1)\}$ , and 4) the vertically integrated liquid water, VIL ( $\text{kg}/\text{m}^2$ ). In the above,  $\rho_{rx}^a(1)$  and  $\rho_{rx}^r(1)$  denote the local spatial correlation of  $r_x$  along the azimuthal and radial directions, respectively, at the separation distance of 1 (bin),  $h_t$  denotes the height of the apparent convective core (km),  $\rho_{ht}^a(1)$  and  $\rho_{ht}^r(1)$  are the same as  $\rho_{rx}^a(1)$  and  $\rho_{rx}^r(1)$ , respectively, but for  $h_t$ . The height of the apparent convective core,  $h_t$ , is defined as the maximum height of the radar reflectivity exceeding some significant reflectivity (an adaptable parameter) at each azran bin. For notational brevity, we denote  $\min\{\rho_{rx}^a(1), \rho_{rx}^r(1)\}$  and  $\min\{\rho_{ht}^a(1), \rho_{ht}^r(1)\}$  as  $\rho_{rx}$  and  $\rho_{ht}$ , respectively. The Z-M relationship used to estimate VIL is the WSR-88D default,  $M=3.44 \times 10^{-6} Z^{4/7}$  where  $Z$  is the reflectivity factor in  $\text{mm}^6/\text{m}^3$  and  $M$  is the liquid water content in  $\text{kg}/\text{m}^3$ . For further details with graphical examples of the attribute fields, the reader is referred to Fulton et al. (2001).

The motivation for using  $r_x$  is to detect convective precipitation regardless of the stage of development of convection. Examination of a large number of volume scans indicates that  $r_x$  works well for identification of convective precipitation as long as little bright band enhancement is present. The motivation for using the spatial statistics of  $r_x$  and  $h_t$  is to detect stratiform precipitation and, in particular, bright band enhancement. The correlation coefficients are examined in both azimuthal and radial directions because, e.g.,  $r_x$  may be better correlated azimuthally than radially in the area of bright band. The correlation coefficients for the  $ij$ -th azran bin are calculated locally over an area that is “ $i$ ” bins-wide azimuthally and “ $j$ ” bins long radially. Sensitivity analysis indicates that a reasonable choice for  $i$  and  $j$  is between 5 and 7 for both  $r_x$  and  $h_t$ . In estimating  $\rho_{rx}$  and  $\rho_{ht}$ , we used the same number of bins regardless of the range, even though the averaging area at a close range is much smaller than that at a far range. Further work is needed to examine the dependence of the local statistics on range, and to assess its impact on CSSA-RCA. Because the azimuthal width of an azran bin is range-dependent, sample spatial correlation coefficients along the azimuthal direction can only be calculated at different physical lag distances. To convert the sample spatial correlation coefficients at varying spatial lag distances to those at the fixed separation distance of 1 km, we assumed that the correlation structure is negative exponential (with no nugget effect).

In practice, the binary decision approach used above to select separation attributes is not very desirable because a single set of thresholds cannot possibly work well consistently and reliably for all sites, all seasons, and under varying conditions of radar calibration accuracy. As such, for the separation algorithm to be operationally viable, it is necessary that the likelihood of a particular azran bin belonging to the convective area be objectively quantified on a continuous scale (rather than binary-mapped). One such commonly used scale is the probability measure, which we adopt here also. The CSSA problem then amounts to estimating the conditional probability that the azran bin in question is in the convective area given the separation attributes observed at that bin; i.e.  $\text{Prob} [\text{Bin} \in \text{convective} | r_x=r_{x0}, \rho_{rx}=\rho_{rx0}, \rho_{ht}=\rho_{ht0}, \text{VIL}=\text{VIL}_0]$ , where

Prob[ ] denotes the probability of the event bracketed occurring, and  $r_{x0}$ ,  $\rho_{rx0}$ ,  $\rho_{ht0}$  and  $VIL_0$  denote the observed values of  $r_x$ ,  $\rho_{rx}$ ,  $\rho_{ht}$  and  $VIL$ , respectively, at that bin.

To estimate the conditional probability, a number of techniques are available; neural network, fuzzy logic, optimal linear estimation, Bayesian estimation, direct empirical estimation, and others. Given the number of separation attributes identified, the difficulty of updating parameters on line due to lack of ground truth, and the importance of producing unbiased estimates, we chose optimal linear estimation based on indicator (i.e., binary) variable transformation. For further discussion on the choice, the reader is referred to Fulton et al. (2001).

### 3. Estimation of Conditional Probability

In this section, we describe how the conditional probability,  $\text{Prob} [\text{Bin} \in \text{stratiform} \mid r_x < r_{xci}, \rho_{rx} \geq \rho_{rxj}, \rho_{ht} \geq \rho_{htk}, VIL < VIL_l; i=1, \dots, n_1, j=1, \dots, n_2, k=1, \dots, n_3, l=1, \dots, n_4]$  is estimated, where  $r_{xi}$ ,  $\rho_{rxj}$ ,  $\rho_{htk}$  and  $VIL_l$  are the  $i$ -th,  $j$ -th,  $k$ -th and  $l$ -th thresholds for  $r_x$ ,  $\rho_{rx}$ ,  $\rho_{ht}$  and  $VIL$ , respectively,  $n_1$ ,  $n_2$ ,  $n_3$  and  $n_4$  denote the number of thresholds used for  $r_x$ ,  $\rho_{rx}$ ,  $\rho_{ht}$  and  $VIL$ , respectively. (Note that  $\text{Prob}[\text{Bin} \in \text{convective} \mid \bullet] = 1 - \text{Prob}[\text{Bin} \in \text{stratiform} \mid \bullet]$ .) The first step is to approximate the above conditional probability with the following conditional expectation involving indicator variables (i.e., the binary encoding of the attributes by applying thresholds):

$$\begin{aligned} & \text{Prob}[\text{Bin} \in \text{stratiform} \mid r_x < r_{xi}, \rho_{rx} \geq \rho_{rxj}, \rho_{ht} \geq \rho_{htk}, VIL < VIL_l; i=1, \dots, n_1, j=1, \dots, n_2, k=1, \dots, n_3, \\ & l=1, \dots, n_4] \\ & \approx E[I_s \mid I_{rxi} = i_{rxi}, I_{prxj} = i_{prxj}, I_{phk} = i_{phk}, I_{VILl} = i_{VILl}; i=1, \dots, n_1, j=1, \dots, n_2, k=1, \dots, n_3, l=1, \dots, n_4] \quad (1) \end{aligned}$$

In Eq.(1), the indicator random variables,  $I_s$ ,  $I_{rxi}$ ,  $I_{prj}$ ,  $I_{phk}$  and  $I_{VILk}$  are defined as:

$$i_s = \begin{cases} 0 & \text{if the bin is in the convective area} \\ 1 & \text{otherwise} \end{cases} \quad (2)$$

$$i_{rxi} = \begin{cases} 1 & \text{if } r_x < r_{xi} \\ 0 & \text{otherwise} \end{cases} \quad (3)$$

$$I_{prxj} = \begin{cases} 0 & \text{if } \rho_{rx} < \rho_{rxj} \\ 1 & \text{if otherwise} \end{cases} \quad (4)$$

$$i_{phk} = \begin{cases} 0 & \text{if } \rho_{ht} < \rho_{htk} \\ 1 & \text{otherwise} \end{cases} \quad (5)$$

$$I_{VILl} = \begin{cases} 1 & \text{if } VIL < VIL_l \\ 0 & \text{otherwise} \end{cases} \quad (6)$$

The conditional expectation of  $I_s$  in Eq.(1) is estimated via the following linear estimator:

$$E[I_s | I_{rx_i} = i_{rx_i}, I_{pr_j} = i_{pr_j}, I_{ph_k} = i_{ph_k}, I_{vill_l} = i_{vill_l}; i=1, \dots, n_1, j=1, \dots, n_2, k=1, \dots, n_3, l=1, \dots, n_4]$$

$$= \sum_{i=1}^{n_1} \lambda_{rx_i} i_{rx_i} + \sum_{j=1}^{n_2} \lambda_{pr_j} i_{pr_j} + \sum_{k=1}^{n_3} \lambda_{ph_k} i_{ph_k} + \sum_{l=1}^{n_4} \lambda_{vill_l} i_{vill_l} \quad (7)$$

where  $\lambda_{rx_i}$ ,  $\lambda_{pr_j}$ ,  $\lambda_{ph_k}$  and  $\lambda_{vill_l}$  denote the weights associated with the indicator variables,  $i_{rx_i}$ ,  $i_{pr_j}$ ,  $i_{ph_k}$  and  $i_{vill_l}$ , respectively. The weights are obtained by solving the following indicator version of ordinary kriging (Deutsch and Journel 1992, Seo 1996):

Minimize;

$$J = E[(I_s - I_s^*)^2 | I_{rx} = i_{rx_i}, I_{pr} = i_{pr_j}, I_{ph} = i_{ph_k}, I_l = i_{vill_l}; i=1, \dots, n_1, j=1, \dots, n_2, k=1, \dots, n_3, l=1, \dots, n_4] \quad (8)$$

subject to;

$$\sum_{i=1}^{n_1} \lambda_{rx_i} + \sum_{j=1}^{n_2} \lambda_{pr_j} + \sum_{k=1}^{n_3} \lambda_{ph_k} + \sum_{l=1}^{n_4} \lambda_{vill_l} = 1 \quad (9)$$

where  $I_s^*$  in Eq.(8) is given by Eq.(7). The above constrained minimization is identical to ordinary kriging, and is referred to in geostatistics as indicator cokriging. The weights in Eq.(9) are obtained by solving the following linear system:

$$\begin{bmatrix} \text{Cov}(I_{rx}, I_{rx}) & \text{Cov}(I_{rx}, I_{pr}) & \text{Cov}(I_{rx}, I_{ph}) & \text{Cov}(I_{rx}, I_{vill}) & U_1^T \\ \text{Cov}(I_{pr}, I_{rx}) & \text{Cov}(I_{pr}, I_{pr}) & \text{Cov}(I_{pr}, I_{ph}) & \text{Cov}(I_{pr}, I_{vill}) & U_2^T \\ \text{Cov}(I_{ph}, I_{rx}) & \text{Cov}(I_{ph}, I_{pr}) & \text{Cov}(I_{ph}, I_{ph}) & \text{Cov}(I_{ph}, I_{vill}) & U_3^T \\ \text{Cov}(I_{vill}, I_{rx}) & \text{Cov}(I_{vill}, I_{pr}) & \text{Cov}(I_{vill}, I_{ph}) & \text{Cov}(I_{vill}, I_{vill}) & U_4^T \\ U_1 & U_2 & U_3 & U_4 & 0 \end{bmatrix} \begin{bmatrix} \lambda_{rx} \\ \lambda_{pr} \\ \lambda_{ph} \\ \lambda_{vill} \\ \mu \end{bmatrix} = \begin{bmatrix} \text{Cov}(I_s, I_{rx}) \\ \text{Cov}(I_s, I_{pr}) \\ \text{Cov}(I_s, I_{ph}) \\ \text{Cov}(I_s, I_{vill}) \\ 1 \end{bmatrix} \quad (10)$$

In the above,  $\mu$  is the Lagrange multiplier,  $U_1$ , e.g., is the  $(1 \times n_1)$  unit vector;  $U_1 = (1, 1, \dots, 1)$ ,  $\text{Cov}(I_s, I_{rx})$ , e.g., is the  $(n_1 \times 1)$  indicator covariance vector;  $\text{Cov}(I_s, I_{rx}) = [\text{Cov}(I_s, I_{rx1}), \dots, \text{Cov}(I_s, I_{rxn1})]^T$ , and  $\text{Cov}(I_{rx}, I_{pr})$ , e.g., the  $(n_1 \times n_2)$  indicator covariance matrix;

$$Cov(I_{rx}, I_{\rho x}) = \begin{bmatrix} Cov(I_{rx_1}, I_{\rho x_1}) & \dots & Cov(I_{rx_1}, I_{\rho x_{n_2}}) \\ Cov(I_{rx_2}, I_{\rho x_1}) & \dots & Cov(I_{rx_2}, I_{\rho x_{n_2}}) \\ \cdot & \dots & \cdot \\ \cdot & \dots & \cdot \\ Cov(I_{rx_{n_1}}, I_{\rho x_1}) & \dots & Cov(I_{rx_{n_1}}, I_{\rho x_{n_2}}) \end{bmatrix} \quad (11)$$

The estimation procedure described above amounts to approximating the multivariate conditional probability in (1) with a set of bivariate conditional probabilities. To illustrate equivalence between indicator covariance and bivariate probability, we may rewrite, e.g.,  $Cov(I_s, I_{VIL_1})$  in  $Cov(I_s, I_{VIL})$  as:

$$\begin{aligned} & Cov(I_s, I_{VIL_1}) \\ &= E[I_s I_{VIL_1}] - E[I_s] E[I_{VIL_1}] \end{aligned} \quad (12a)$$

$$= \text{Prob}[ \text{Bin} \in \text{stratiform}, VIL < VIL_1 ] - \text{Prob}[ \text{Bin} \in \text{stratiform} ] \text{Prob}[ VIL < VIL_1 ] \quad (12b)$$

$$= \{ \text{Prob}[ \text{Bin} \in \text{stratiform} \mid VIL < VIL_1 ] - \text{Prob}[ \text{Bin} \in \text{stratiform} ] \} \text{Prob}[ VIL < VIL_1 ] \quad (12c)$$

Note in (12c) that, if VIL is indeed a skillful attribute for differentiating convective precipitation from stratiform, the conditional probability,  $\text{Prob}[ \text{Bin} \in \text{stratiform} \mid VIL < VIL_1 ]$ , would be greater than the unconditional,  $\text{Prob}[ \text{Bin} \in \text{stratiform} ]$ , thus resulting in a positive indicator covariance. It can be easily shown that, if there is only one attribute available (e.g. VIL) and only one threshold (e.g.  $VIL_1$ ) is used, the estimation procedure described above reduces to applying the threshold directly; i.e., the azran bin is in the convective area if  $VIL \geq VIL_1$ , and in the stratiform region if  $VIL < VIL_1$ .

The estimation procedure described above requires specification of the indicator statistics in (10). Ideally, the statistics should come from a large sample in a site- and seasonality-specific manner. In reality, because estimation of the indicator statistics in the right-hand side of (10) requires ground-truth (i.e. identification of areas of ‘true’ convective precipitation: see (2)), large sample estimation of indicator statistics is not operationally viable. As such, the approach taken here is to estimate the indicator statistics from a small but very informative sample. Such a sample should contain, in the least, a precipitation event with widespread, well-developed and clearly distinguishable areas of convective and stratiform precipitation. For that, we used the southern plains squall line at KINX (Tulsa, OK) on May 9, 1995. The particular data set used includes four volume scans that are approximately an hour apart, and covers the passage of the precipitating system from entry into through exit from the radar’s field of view. Fig. 1 shows the field of maximum reflectivity,  $r_x$ , for one of the volume scans. Note in the figure the very well developed convective front and trailing stratiform region. To estimate the indicator statistics involving  $I_s$  in the right-hand side of (10), it is necessary to determine the “true” area of convective precipitation. Here, we considered the area containing the convective front separated by the solid black line to be the true area of convective precipitation. Figs 2 through 5 show the

$\rho_{rx}$ ,  $h_t$ ,  $\rho_{ht}$ , VIL fields corresponding to Fig 1. Note in Figs 1 through 5 that the area of stratiform precipitation is characterized by small  $r_x$ , large  $\rho_{rx}$ , lack of spatial variability in  $h_t$ , large  $\rho_{ht}$ , and small VIL. In the  $\rho_{rx}$  field of Fig 2, the discontinuities seen in the area of stratiform precipitation are sampling artifacts due to coarse elevation angles in the Volume Coverage Pattern (VCP) of the radar.

The thresholds,  $r_{xi}$ ,  $\rho_{rxj}$ ,  $\rho_{htk}$ ,  $VIL_l$ ;  $i=1,\dots,n_1$ ,  $j=1,\dots,n_2$ ,  $k=1,\dots,n_3$ ,  $l=1,\dots,n_4$ , in Eq.(1) were specified from a series of sensitivity analysis consisting of the following steps: 1) assume a number of thresholds for each attribute, 2) assume threshold settings, 3) estimate the indicator statistics, 4) estimate the conditional probability maps for all volume scans, 5) examine the results, 6) repeat Steps 1 through 5 until the conditional probability maps exhibit the most skill in discriminating convective precipitation from stratiform. For further details, the reader is referred to Seo et al. (2002). Based on the analysis, we chose three thresholds for each attribute and the following settings for the thresholds;  $i_{rxj} = 38, 40, 42$  (dBZ);  $i_{\rho rj} = 0.97, 0.98, 0.99$ ;  $i_{\rho hj} = 0.900, 0.990, 0.999$ ;  $i_{VILj} = 5.5, 6.0, 6.5$  (kg/m<sup>2</sup>), for  $j=1,2,3$ . Fig 6 shows the resulting conditional probability map obtained from Figs 1, 2, 4 and 5 via the optimal linear estimation procedure described above. Note that the convective front is characterized by higher levels of probability, an indication that the probability map possesses a rather high level of separation skill. The absolute magnitude of the conditional probabilities seen in Fig 6 depends on the reflectivity morphology in the particular data set used to estimate the indicator statistics. As such, the threshold probability, above which precipitation is classified as convective, may be chosen either interactively via visual examination of the probability maps or by maximizing the performance measures of choice via sensitivity analysis. In this work, we chose a threshold probability of 0.8 based on visual examination of the dependent case (May 9, 1995, KINX). The same threshold probability is then used throughout the independent evaluation described below.

#### 4. Evaluation

To evaluate the performance of CSSA, we ran CSSA and RCA for 22 cases of considerable diversity (see Table 1). For all cases, we used the threshold settings and indicator statistics obtained from the previous section. For each case, the independent validation of CSSA involved the following steps: 1) perform convective-stratiform separation using CSSA, 2) estimate the mean vertical profile of reflectivity (VPR) using the volume scan reflectivity data within the area identified as stratiform, 3) apply the correction factors derived from the mean VPR to the raw reflectivity data in the stratiform area only, 4) convert reflectivity to rainfall in all areas using a single Z-R relationship and accumulate in time, 5) repeat the above steps for all volume scans over the period of interest. To evaluate CSSA quantitatively, one would have like the “true” convective-stratiform fields delineated objectively using, e.g., observations from polarimetric radar. In reality, however, we only had the WSR-88D reflectivity data. By visually examining the separation results against the reflectivity morphology observable from the volume scan data, rigorous qualitative evaluation is nevertheless possible. In Figs 7 through 12, we show the  $r_x$  and the corresponding conditional probability maps for 6 cases from Table 1. For additional graphics for these and other cases, the reader is referred to Seo et al. (2002, 2003). The figures show that, in general, CSSA performs very well for the continental-type mixed precipitation events. Due to the dependence of the separation attributes on range and sampling density of the elevation angle, however, the separation skill diminishes at far ranges, and may not be of the

same quality over certain ranges where volume coverage is sparser. Also, due to the sensitivity of the separation attributes to data quality, unrealistic patterns of probability may occasionally occur in areas where outliers exist. For the hurricane event (Opal at KEVX, Fig 8), which has rather different VPRs than continental convective precipitation, CSSA tends to under-identify convective precipitation, an issue that will be revisited later in this section.

Another way to evaluate the performance of CSSA is to examine the VPRs (i.e. the location-specific, individual vertical profiles of reflectivity, rather than their spatial mean) sampled from the area identified as stratiform. Note that, if CSSA is successful, the VPRs sampled from the stratiform area should exhibit relatively small variability (i.e. the individual VPRs should bundle up tightly). To illustrate this, we used VIL-only CSSA as a point of comparison with the four-attribute CSSA described above. In VIL-only CSSA, only VIL is used as the sole separation attribute in the optimal linear estimation procedure. As may be seen in Figs 5, VIL is generally a rather skillful attribute for convective-stratiform separation, but tends to under- and over-identify areas of convective and stratiform precipitation, respectively. Figs 13a through 15a show examples of the VPRs sampled from the areas of stratiform precipitation as identified by VIL-only CSSA. Figs. 13b through 15b are the same as Figs 13a through 15a, except that all four attributes are used in CSSA instead. Note that the VPRs from VIL-only CSSA show a significantly large number of reflectivity values that are outside of the tightly clustered stratiform VPRs. Those from the full CSSA, on the other hand, show the clusters of stratiform VPRs with significantly fewer reflectivity values from convective precipitation.

While the above evaluations are very useful in assessing the performance of CSSA for convective-stratiform separation itself, they do not necessarily assess the value of CSSA in radar QPE. For that, we compare the radar rainfall maps corrected by CSSA-RCA with the uncorrected. Figs 16a through 21a show radar rainfall maps without CSSA-RCA correction for 6 cases in Table 1. Figs 16b through 21b show the matching radar rainfall maps with CSSA-RCA correction. In generating radar rainfall accumulation maps, the convective Z-R relationship ( $Z=300R^{1.4}$ , Z in  $\text{mm}^6/\text{m}^3$  and R in mm/hr) and a hail cap of 56 dBZ were used everywhere in the radar umbrella throughout the accumulation duration. The only exception is in Fig 20 (Hurricane Opal), for which the tropical Z-R relationship ( $Z=250R^{1.2}$ ) is used. Note in Fig 16 that, for a mixed precipitation event such as this squall line, CSSA does the intended job very well: little or no adjustment is made to convective precipitation while significantly reducing brightband enhancement in stratiform precipitation (see Seo et al. 2003 for graphical display of rainfall amounts added or subtracted by CSSA-RCA). While this type of visual evaluation can only be qualitative by nature, it does reveal a great deal of information about the performance of CSSA-RCA that cannot be gleaned from quantitative comparison with rain gauge data. In particular, rainfall patterns at very far ranges are very often a telltale indicator of the performance of CSSA-RCA. For example, spatially widening and narrowing rainfall patterns along the range are very likely an indication of over- and under-correction, respectively. CSSA-RCA should produce rainfall maps at very far ranges that look physically realistic and are consistent with the rainfall patterns elsewhere. Realistic rainfall patterns at very far ranges are a strong indication that correction at other ranges is very likely to be accurate. Fig 17 illustrates the above points. Though the rainfall patterns at the extreme far ranges in the northeastern quadrant still show missing precipitation due to lack of detection (see Seo et al. 2003), the rainfall patterns elsewhere look physically realistic and consistent over the entire radar umbrella. Fig 18 shows that, for a

mostly convective event, the rainfall map from CSSA-RCA correction is not very much different from that without correction, except at far ranges. Fig 19 is another illustration of how CSSA-RCA may impact radar estimation of stratiform rainfall. While the absolute accuracy of the corrected rainfall maps may not be assessed without comparison with rain gauge data, it does provide an assessment of the magnitude of uncertainty in stratiform radar QPE due to the VPR effects. For a hurricane event (see Fig 20), all VPRs are of convective type. As such, convective-stratiform separation does not apply until the precipitation system takes on continental character well after landfall. Note that, with the indicator statistics derived from a mixed precipitation event, CSSA misidentifies a large area as stratiform (see Fig 8). For this reason, CSSA is not to be used with RCA for pure tropical events. The rainfall map shown in Fig 20b is based on RCA without CSSA. Note that the corrected map is physically realistic and consistent across all ranges.

## **5. Relationship Between Cloud-To-Ground Lightning and Convection Probability**

Though the CSSA is designed to identify all convective-type profiles and not only those with deep convection, we were able to partly validate its ability to identify deep convection through a comparison with cloud-to-ground (CG) lightning observations.

Convective probabilities from 21 volumetric scans were interpolated to a 4-km Cartesian grid centered on the radar site, and collated with CG strikes in the same boxes during a 20-minute window centered on the nominal volumetric scan time. Data were taken from sites KRTX, KTLX, KPBZ, and KRLX between April 20 and May 27, 2004. All cases included some precipitation, and total CG strike counts ranged from < 50 to over 1300, though a few had no lightning. In our statistical analysis, one grid box in one image contributes one case to the sample. A total of 104,000 cases with CPROB > 0 and/or composite reflectivity  $\geq 5$  dBZ were included in the final analysis; of these 2.2% had CG lightning.

As shown in Fig. 22, there was a striking relationship between CPROB and lightning relative frequency, with probabilities under 30% being associated with lightning relative frequency of 2% or less, and probabilities of 90% or higher being associated with lightning relative frequency of 20-50%. Overall, CPROB explained approximately 28% of the variance in lightning. By comparison, composite reflectivity explained only 18% of the variance.

We caution that CSSA is not intended as a radar detection algorithm for lightning. This experiment only demonstrates a relationship between the radar predictors and the depth and intensity of convection, which is in turn correlated with the probability of CG lightning.

## **6. Conclusions and Future Research Recommendations**

An automatic algorithm for identification of convective and stratiform precipitation based on volume scan radar reflectivity data, referred to as the Convective-Stratiform Separation Algorithm (CSSA, Seo et al. 2002), has been developed to support real-time correction of range-dependent biases in radar Quantitative Precipitation Estimation (QPE). The algorithm has been extended to include vertically-integrated liquid water (VIL) as an additional predictor attribute. The resulting 4-attribute CSSA is evaluated in multiple case studies by feeding the separation

results to the Range-dependent bias Correction Algorithm (RCA, Seo et al. 2000). Because VIL is an existing WSR-88D product, VIL-only based stratiform-convective separation, if found viable, may be a significantly less expensive alternative to the full CSSA. To assess performance of the VIL-only CSSA, the two are inter-compared in the multiple case studies.

The major conclusions and recommendations drawn from this work are as follows:

- The Convective-Stratiform Separation Algorithm (CSSA) appears physically realistic, based on its performance in a selected set of cases and its strong correlation with cloud-to-ground lightning events.
- Performance of the Range-dependent bias Correction Algorithm (RCA) is sensitive to that of the Convective-Stratiform Separation Algorithm (CSSA). For RCA to operate as an all-season and all-storm type application, reliable high-level performance of CSSA is essential.
- Performance of the ‘full’ CSSA, which uses four different attributes as predictors, is generally satisfactory whereas that of the ‘VIL-only’ CSSA, which uses VIL as the sole predictor, is not. As such, implementation of the VIL-only CSSA as an interim alternative is not recommended.
- Range dependency of the predictor attributes is found to be one of the factors adversely affecting the performance of CSSA. Improvements are recommended to reduce such range dependency and to employ efficient computational schemes for evaluation of local-statistical attributes.
- Though the performance of CSSA is generally satisfactory for a wide range of storms, it is less robust for certain types of storms, including purely tropical and purely convective. Further case studies, both historical and real-time, are recommended to mature the algorithm and the operations concept and to develop specific operational guidance.

## REFERENCES

- Deutsch, C. V., and Journel, A. G., 1992: GSLIB Geostatistical software library and user's guide. Oxford University Press.
- Fulton, R., D. Miller, J. Breidenbach and D.-J. Seo, 2001: Final Report Interagency MOU among the NEXRAD Program, The WSR-88D Radar Operations Center, and The NWS Office of Hydrologic Development. Hydrology Laboratory, Office of Hydrologic Development, National Weather Service, Silver Spring, MD.
- Seo, D.-J., 1996: Nonlinear estimation of spatial distribution of rainfall - An indicator cokriging approach. *Stoch Hydrol Hydraul*, 10, 127-150.
- Seo, D.-J., J. P. Breidenbach, R. A. Fulton, D. A. Miller, and T. O'Bannon, 2000: Real-time adjustment of range-dependent biases in WSR-88D rainfall data due to nonuniform vertical profile of reflectivity, *J. Hydrometeorol.*, 1(3), 222-240.
- Seo, D.-J., F. Ding and R. Fulton, 2002: Final Report Interagency MOU among the NEXRAD Program, The WSR-88D Radar Operations Center, and The NWS Office of Hydrologic Development. Hydrology Laboratory, Office of Hydrologic Development, National Weather Service, Silver Spring, MD.
- Smith, J. A., D.-J. Seo, M. L. Baeck, and M. D. Hudlow, 1996: An intercomparison study of NEXRAD precipitation estimates. *Water Resour. Res.*, 32, 2035-2045.

Table 1. Description of precipitation cases used in this study

Call Letter	Site	Tape #	Period	Storm Type	Used For
KAMA	Amarillo, TX	N04248	5/30/95	squall line	validation
KATX	Seattle, WA	N10814	2/2/96	stratiform	validation
KDDC	Dodge City, KS	N01158	7/14/93	organized-convective	validation
KEVX	Eglin AFB, FL	N09652	10/4/95	hurricane (Opal)	validation
KFDR	Frederick, OK	N01114	5/9/93	squall line	validation
KFWS	Forth Worth, TX	N02983	4/18/95	squall line	validation
KHGX	Houston, TX	N02961	10/17/94	organized-convective	validation
KICT	Wichita, KS	N02075	4/28/94	squall line	validation
KINX	Tulsa, OK	N04206	5/8/95	squall line	estimation
KMLB	Melbourne, FL	A20054	3/25/92	chaotic-convective	validation
KOKX	New York, NY	N23993	10/19/96	stratiform	validation
KRTX	Portland, OR	N12384	2/6/96	stratiform	validation
KLWX	Sterling, VA		11/29/03	convective, stratiform	validation
KTLX	Norman, OK		1/5/02	stratiform	validation
KFWS	Forth Worth, TX		1/5/02	stratiform	validation
KJAX	Jacksonville, FL		8/1/02	convective	validation
KRTX	Portland, OR		1/24/04	stratiform	validation
KRTX	Portland, OR		1/28/04	stratiform	validation
KRTX	Portland, OR		3/25/04	stratiform	validation
KLZK	Little Rock, AR		1/6/02	stratiform	validation
KHGX	Houston, TX		1/5/02	stratiform	validation
KJAN	Jackson, MS		1/6/02	stratiform	validation

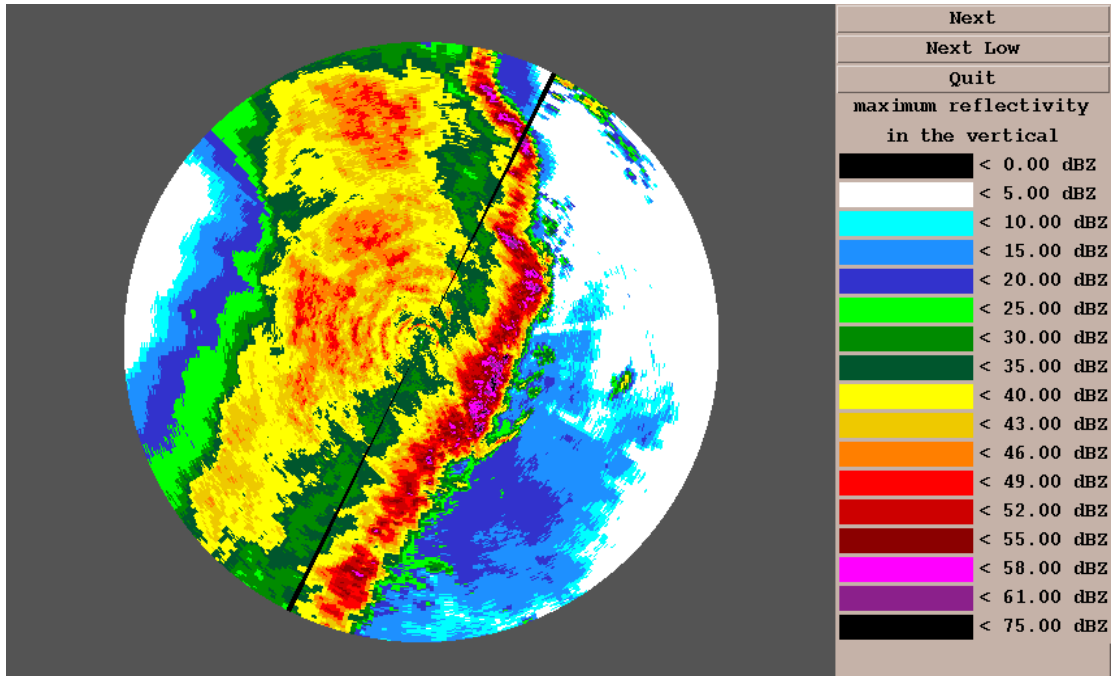


Figure 1. Maximum reflectivity in the vertical (dBZ), from KINX, 9 May 1995.

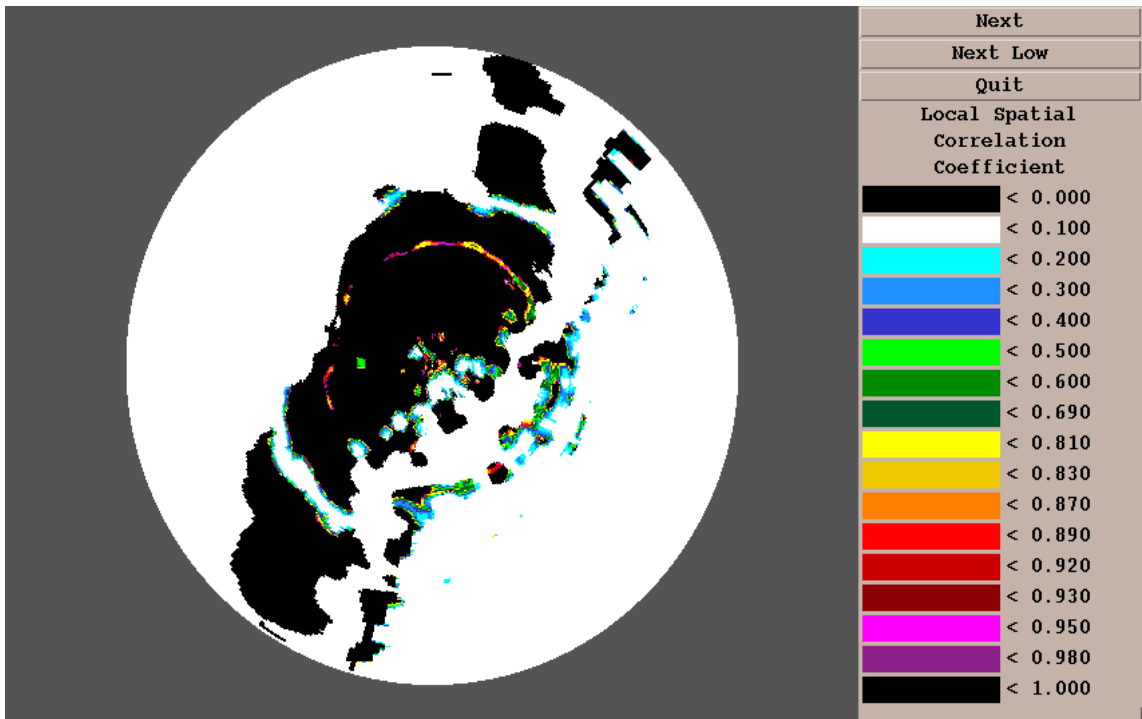


Figure 2. Local horizontal spatial correlation in reflectivity, for case shown in Fig. 1.

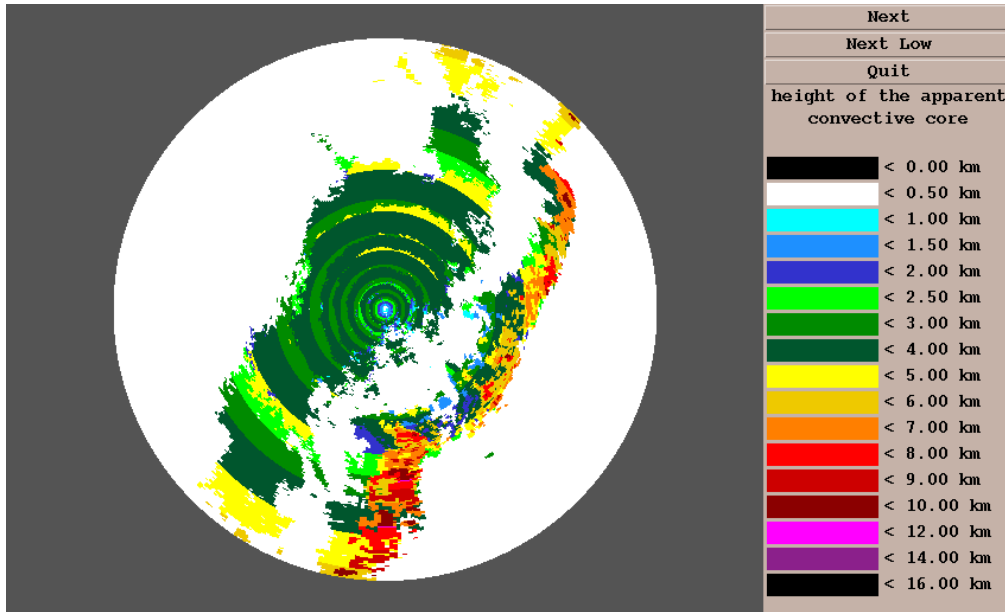


Figure 3. Height of apparent convective core, km AGL, for case in Fig. 1.

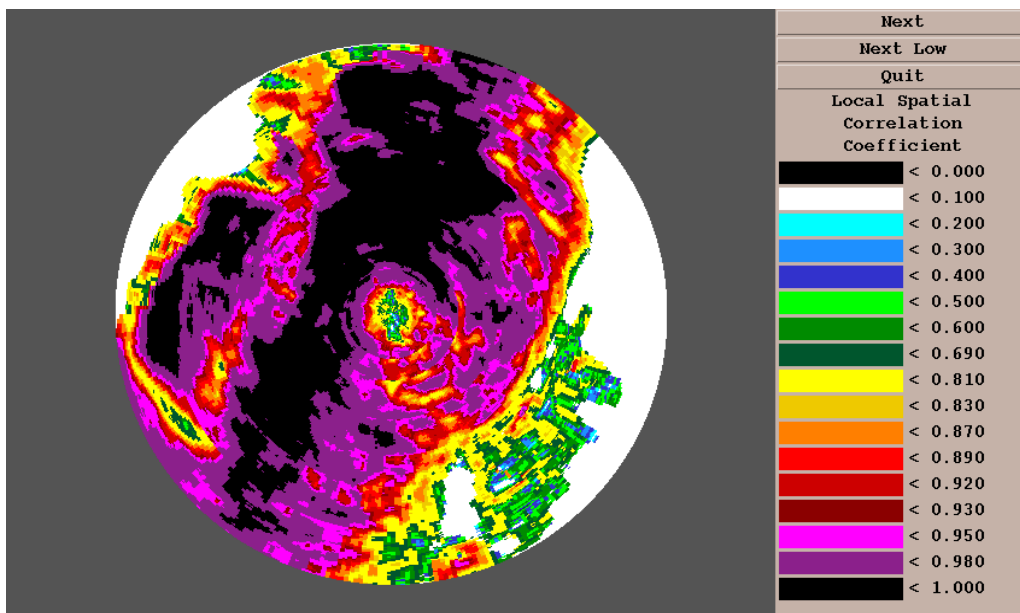


Figure 4. Spatial correlation in height of convective core, for case in Fig. 1.

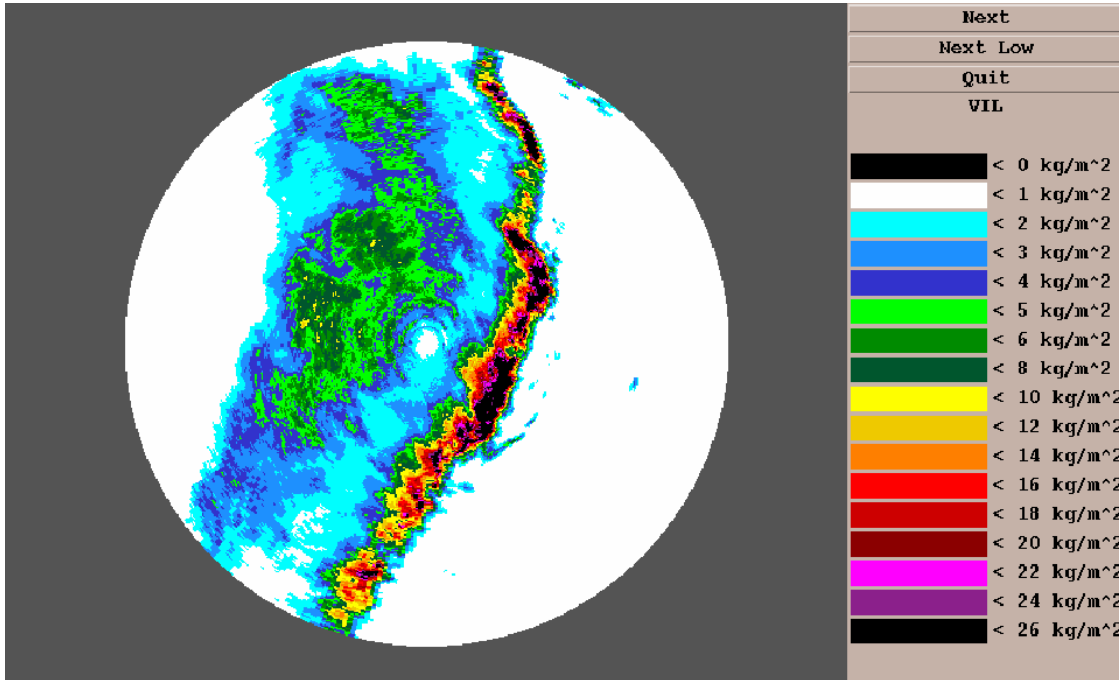


Figure 5. Vertically-integrated liquid (VIL), kg m<sup>-2</sup>, for case in Fig. 1.

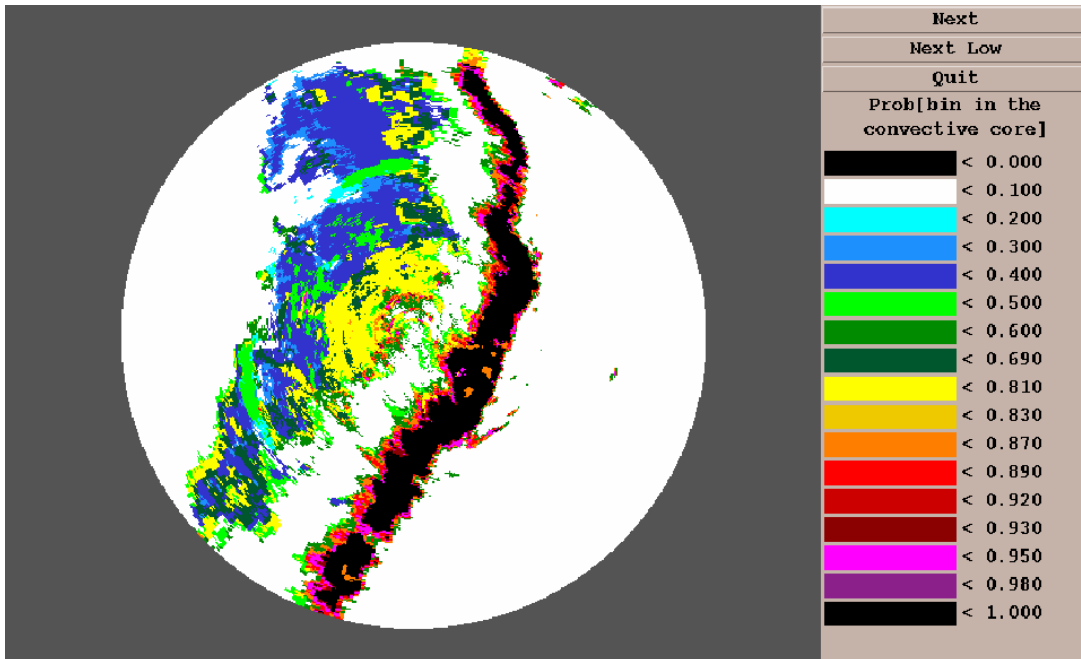


Figure 6. Convective probability based on data illustrated in Figs. 1-5.

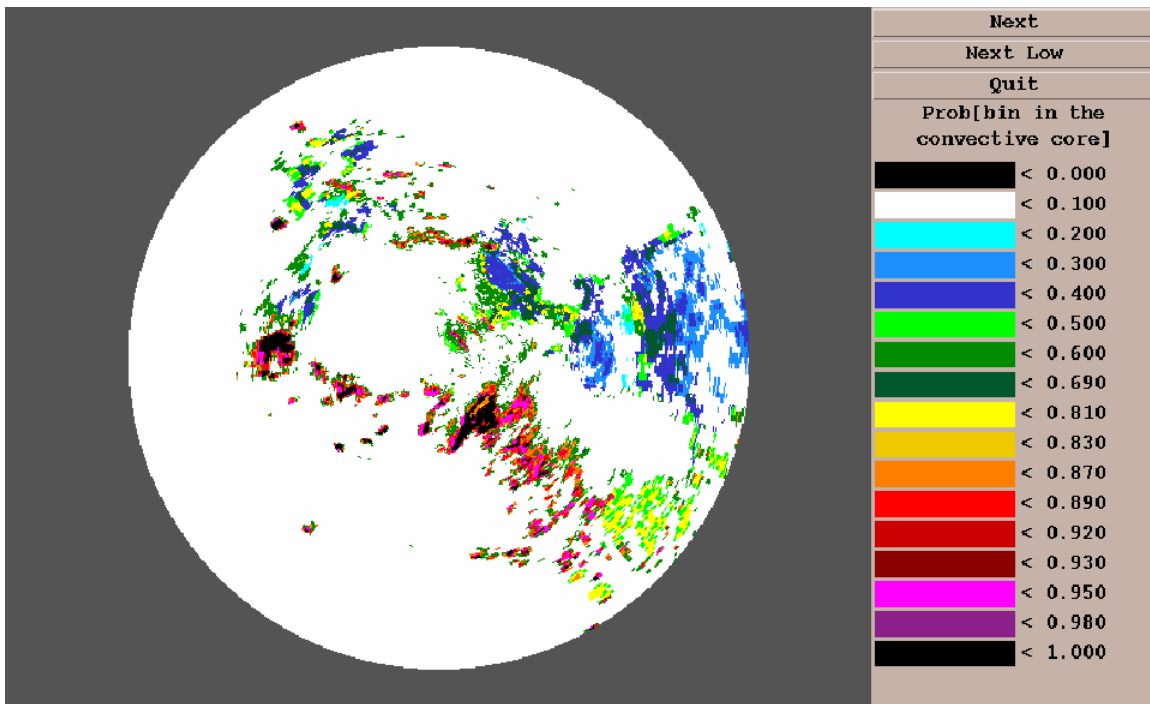
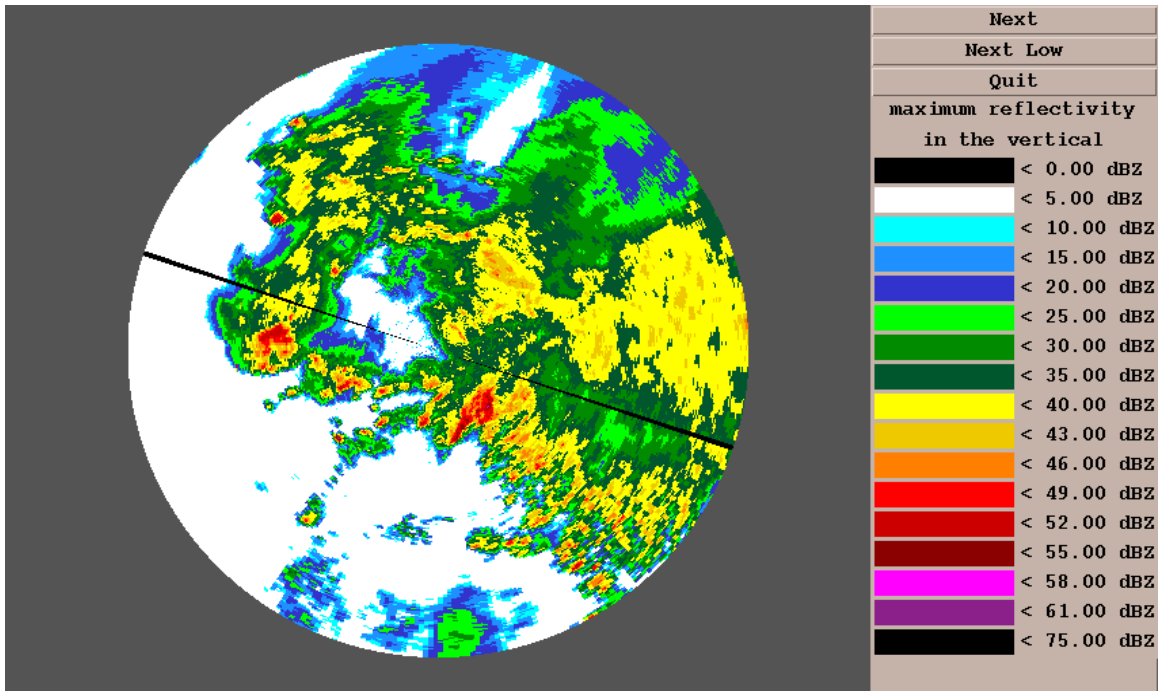


Figure 7. Composite reflectivity (top) and convective probability (bottom).from KDDC, Jul 14, 1993

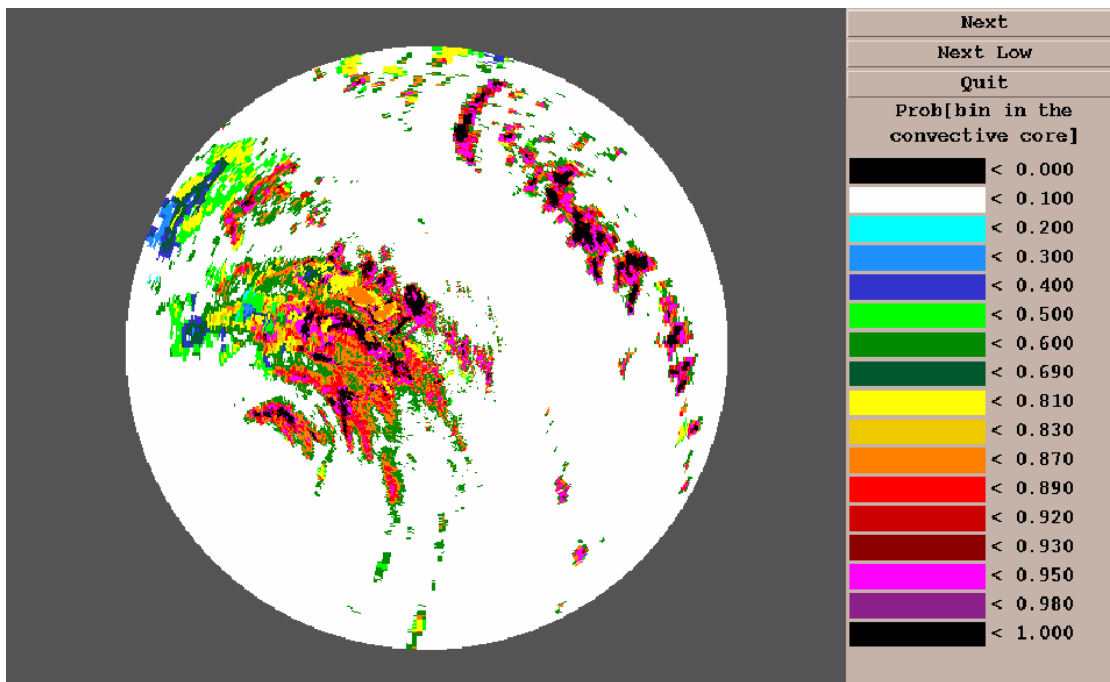
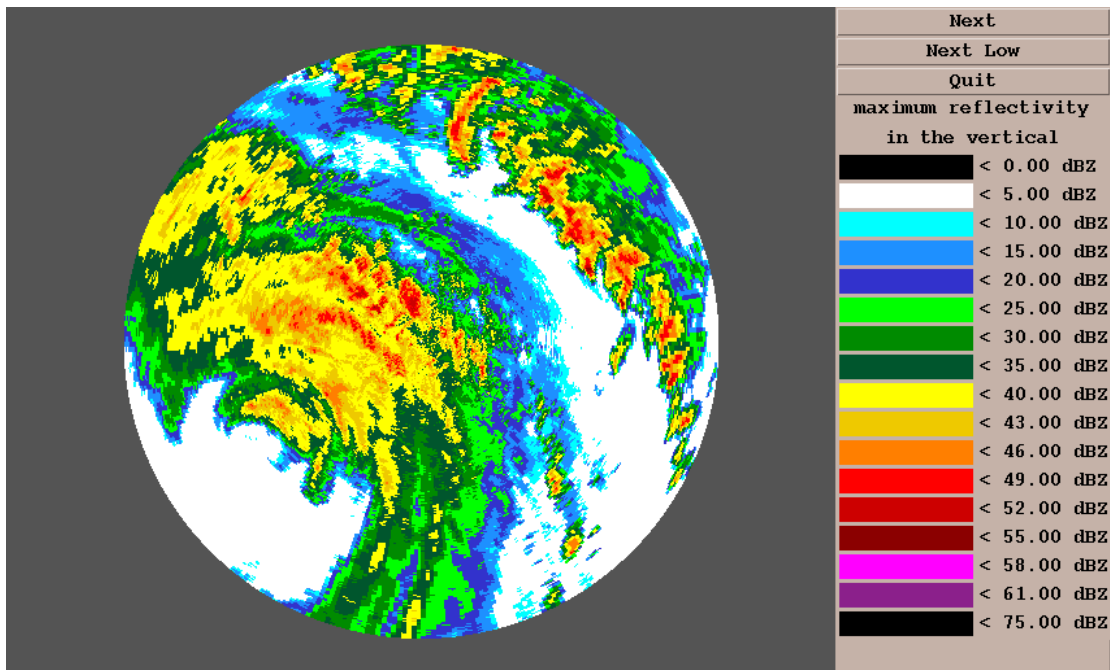


Figure 8. Composite reflectivity (top) and convective probability (bottom).from KEVX, Oct 4, 1995

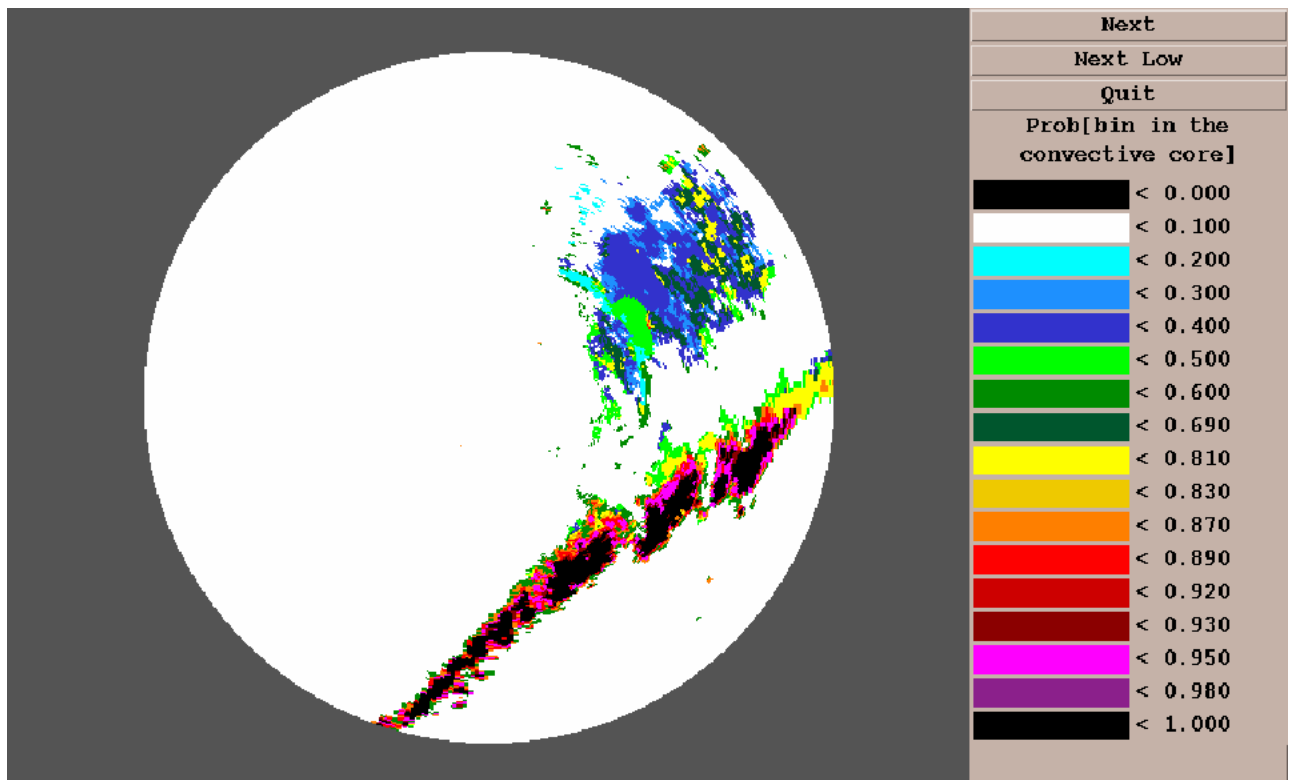
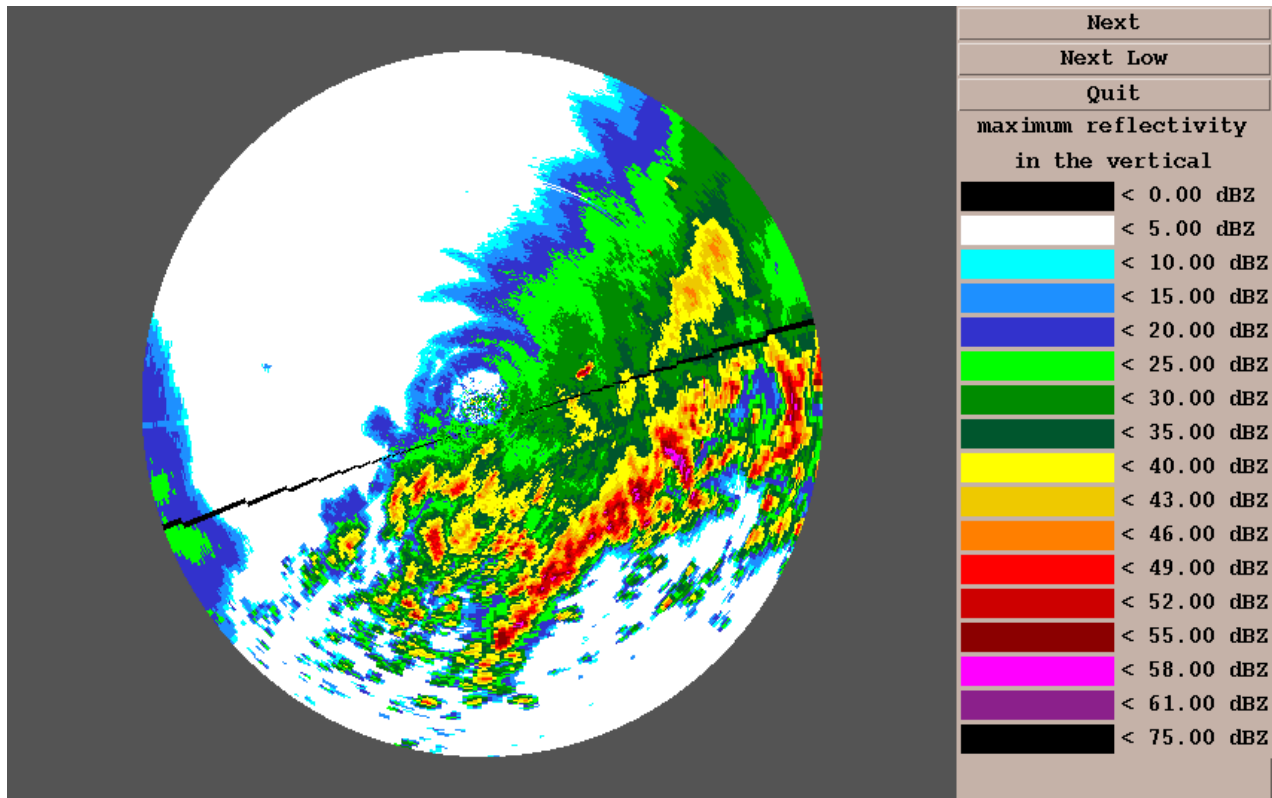


Figure 9. Composite reflectivity (top) and convective probability (bottom).from KFDR, May 9, 1993

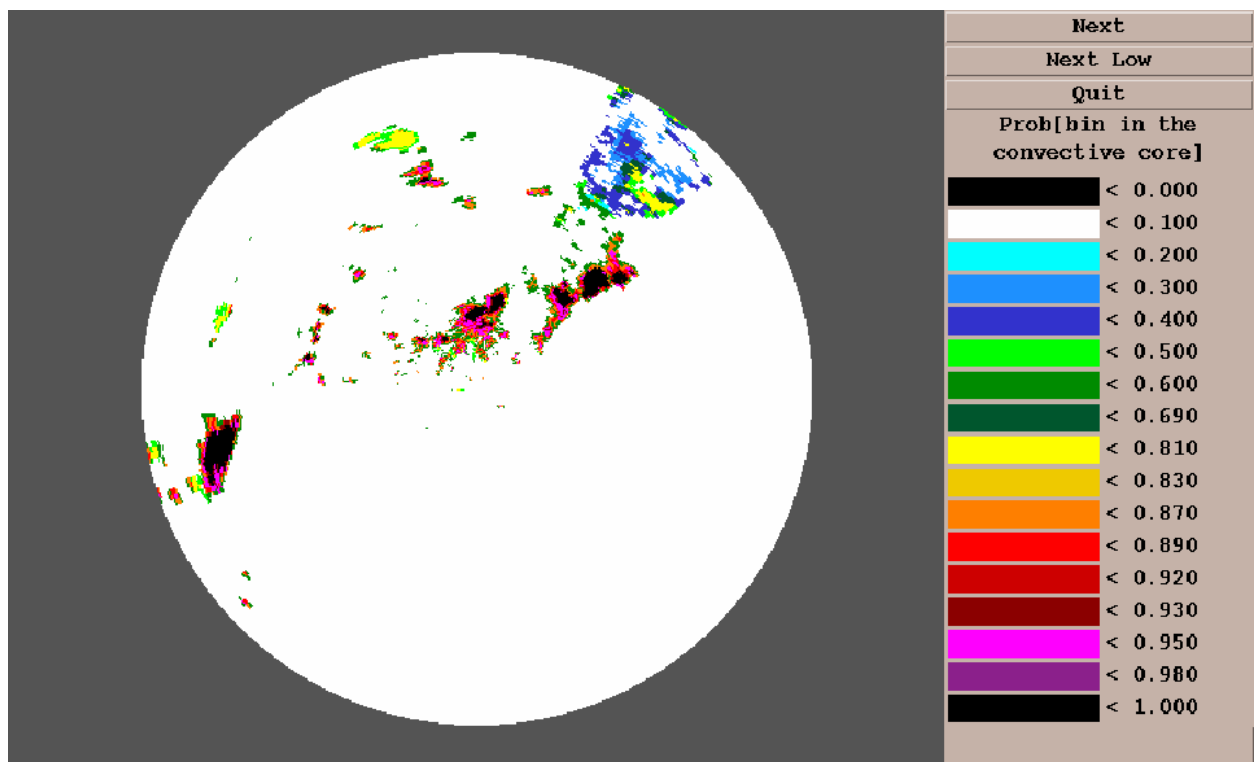
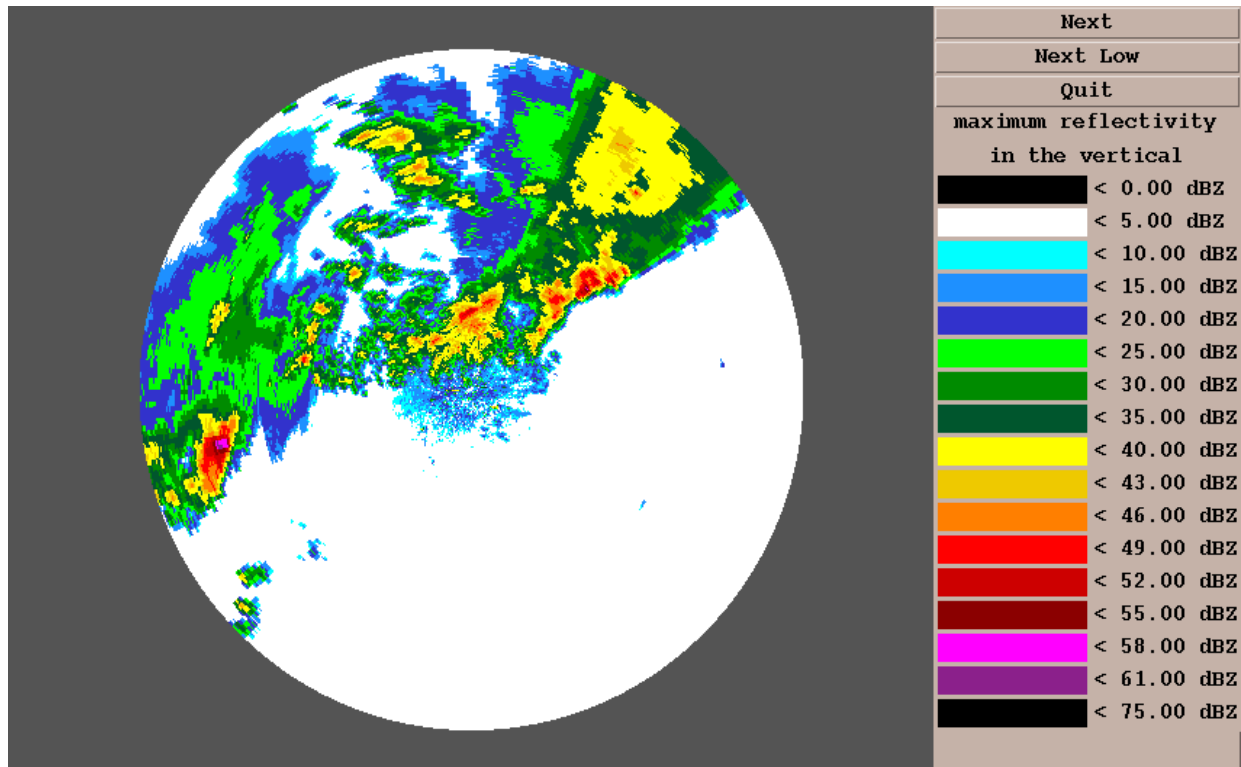


Figure 10. Composite reflectivity (top) and convective probability (bottom).from KHXG, Oct 17, 1994

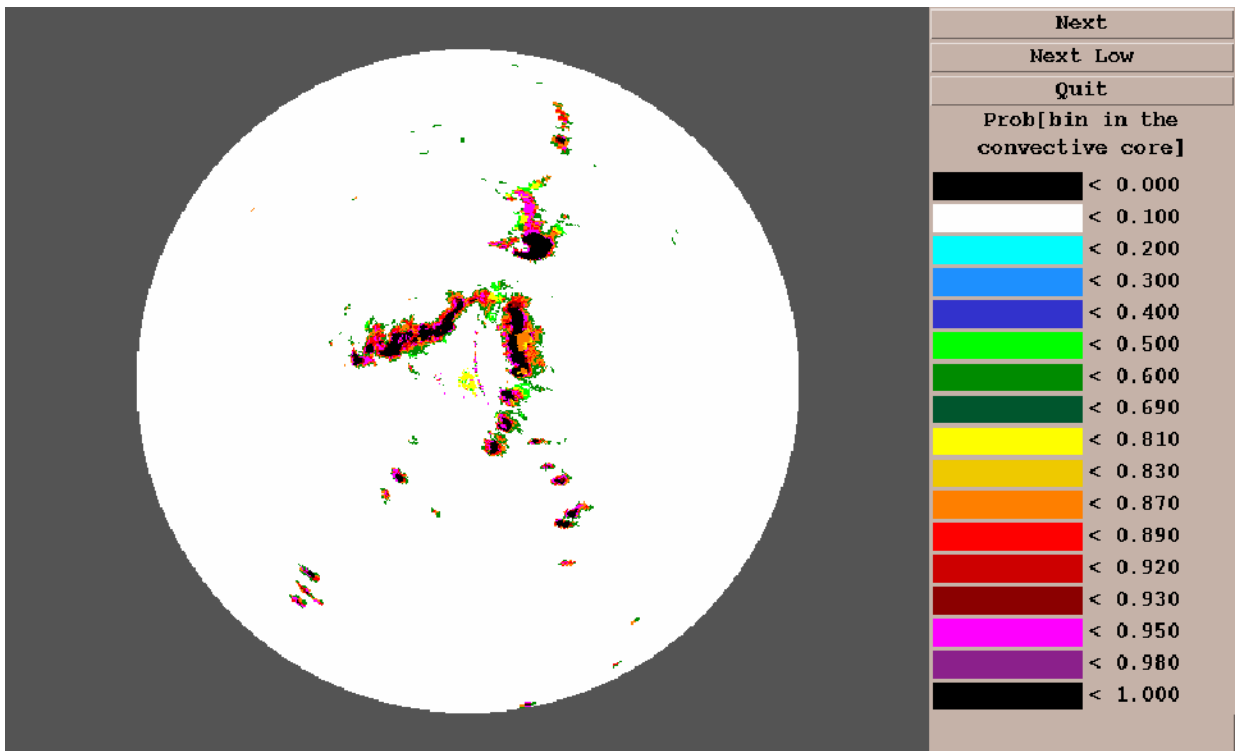
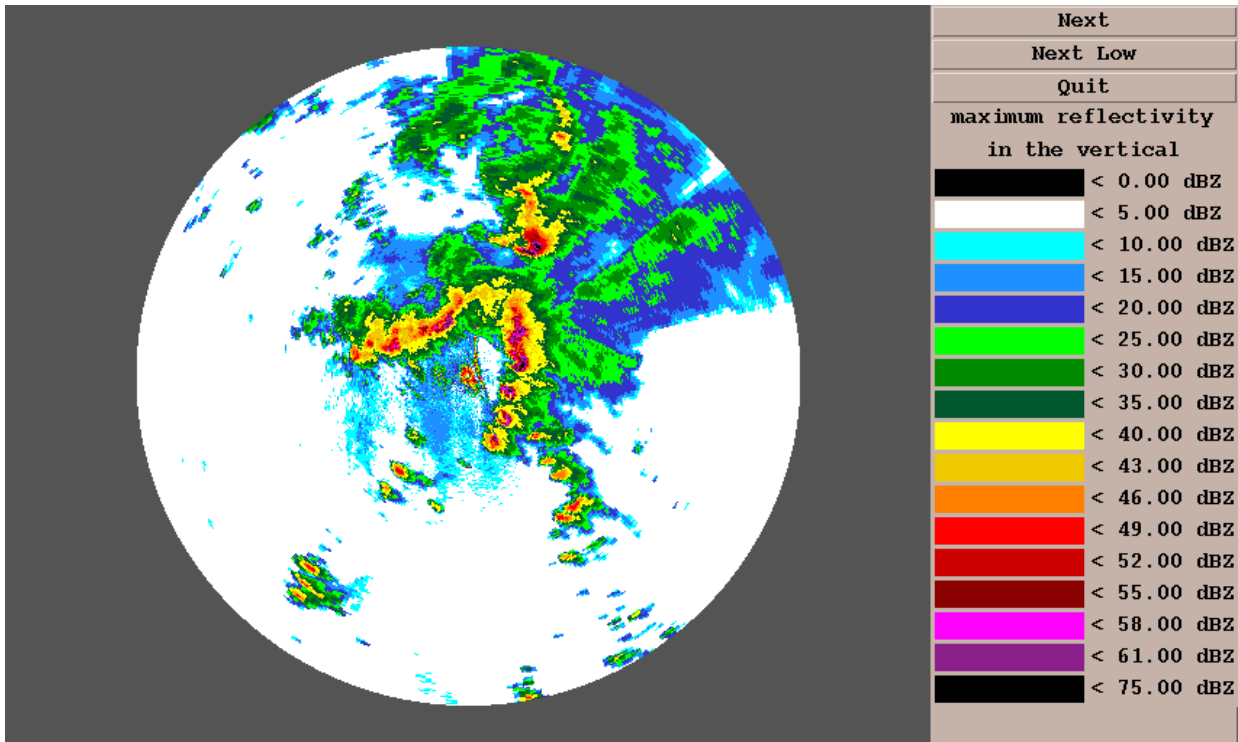


Figure 11. Composite reflectivity (top) and convective probability (bottom).from KMLB, Mar 25, 1992

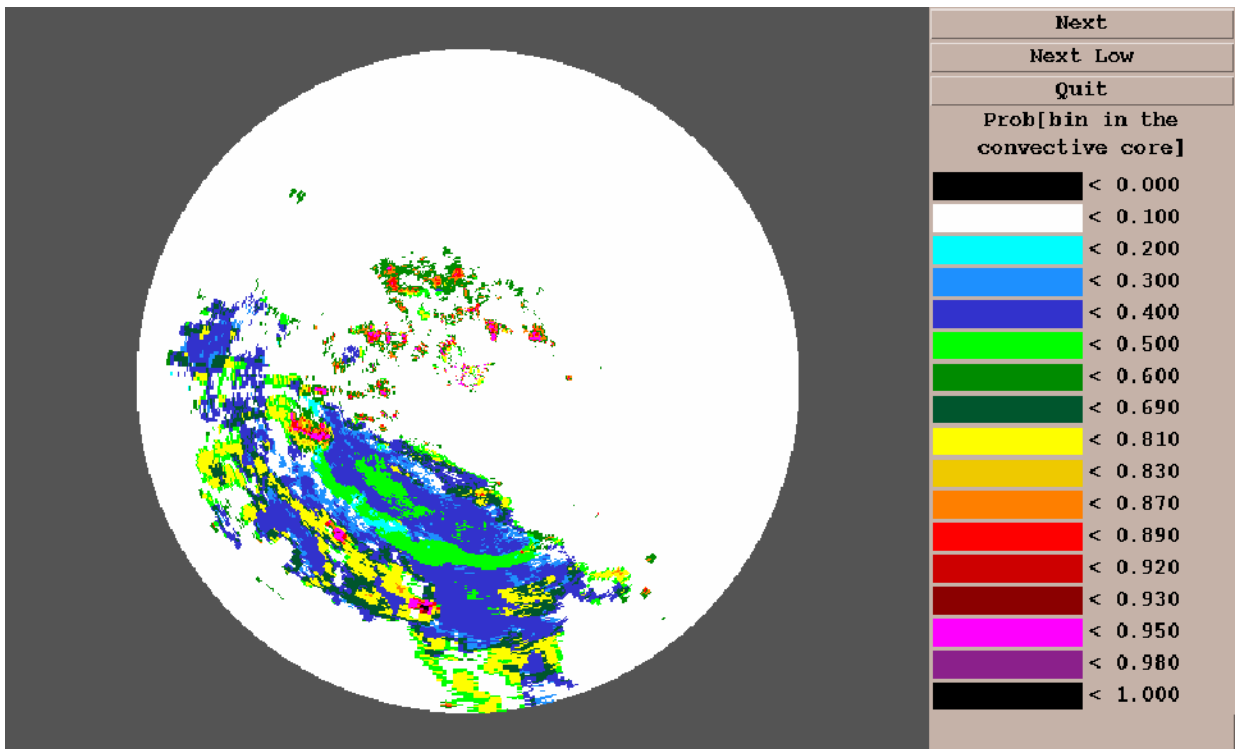
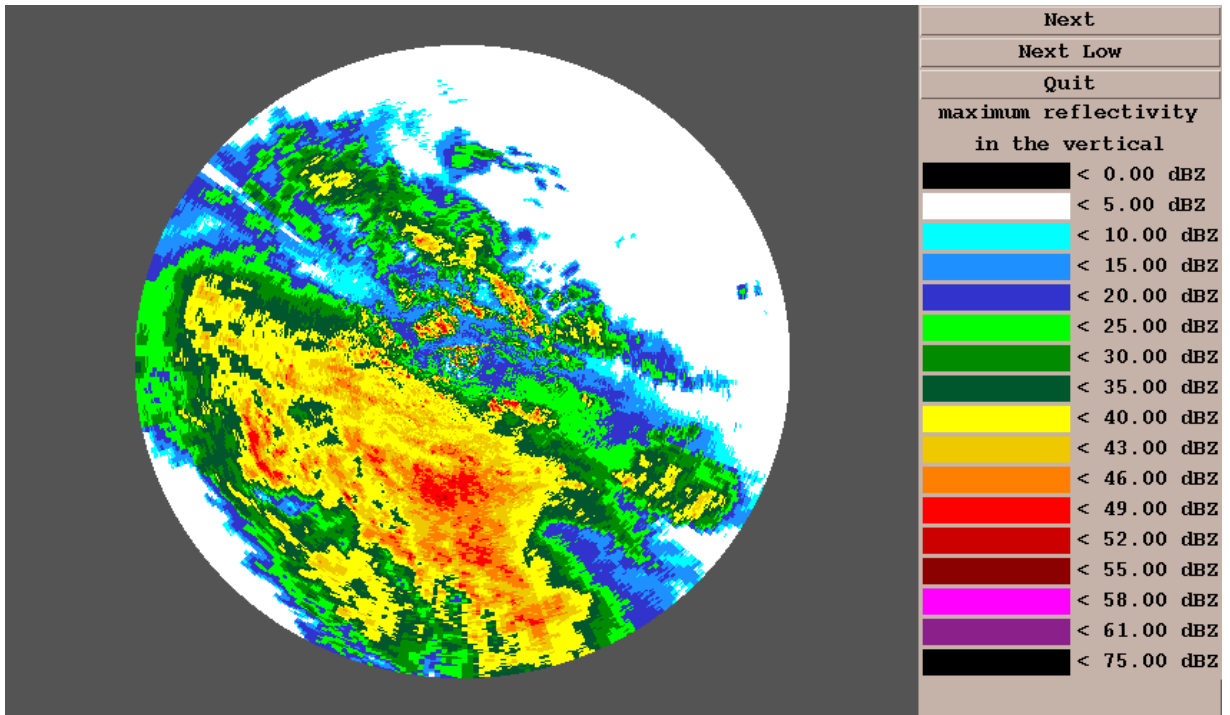


Figure 12. Composite reflectivity (top) and convective probability (bottom) from KOXK, Oct 19, 1996

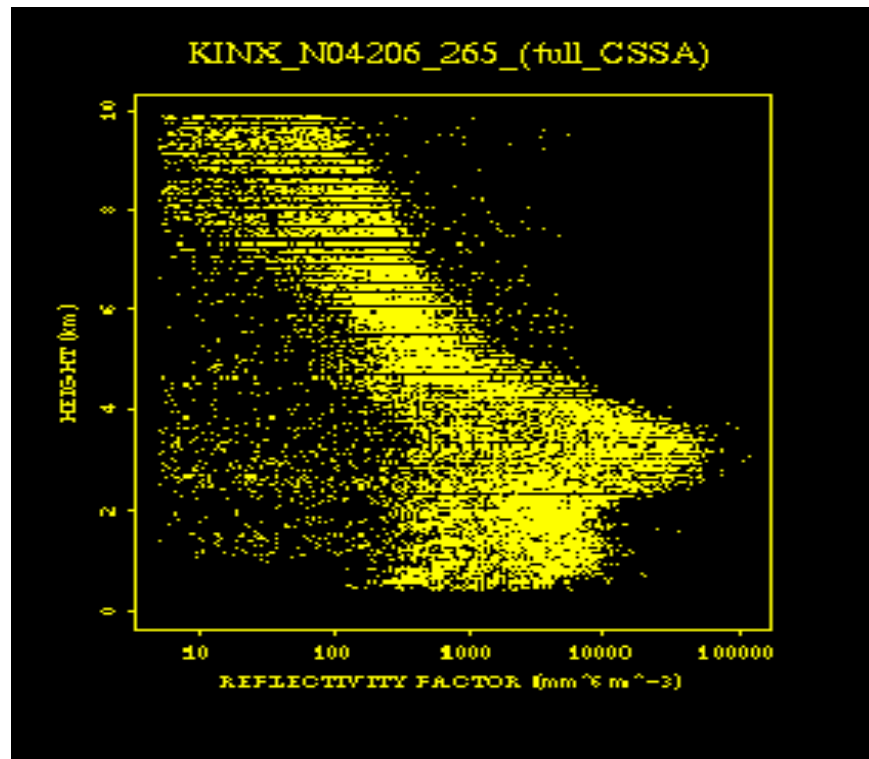
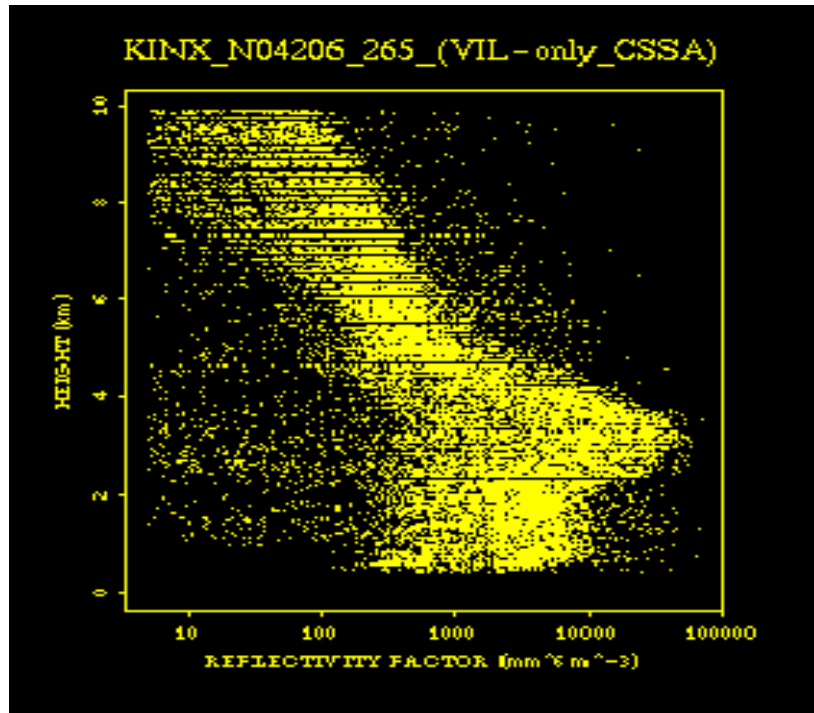


Figure 13. Reflectivity/height scatter plots with (top) VIL-only CSSA and (bottom) full CSSA for KINX (Tulsa OK), 8 May 1995.

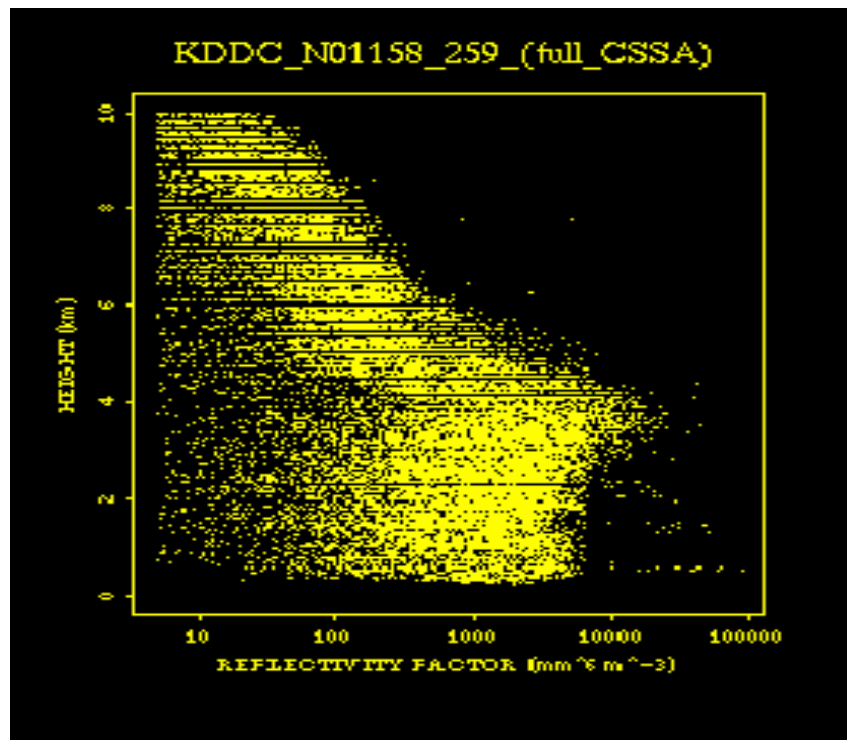
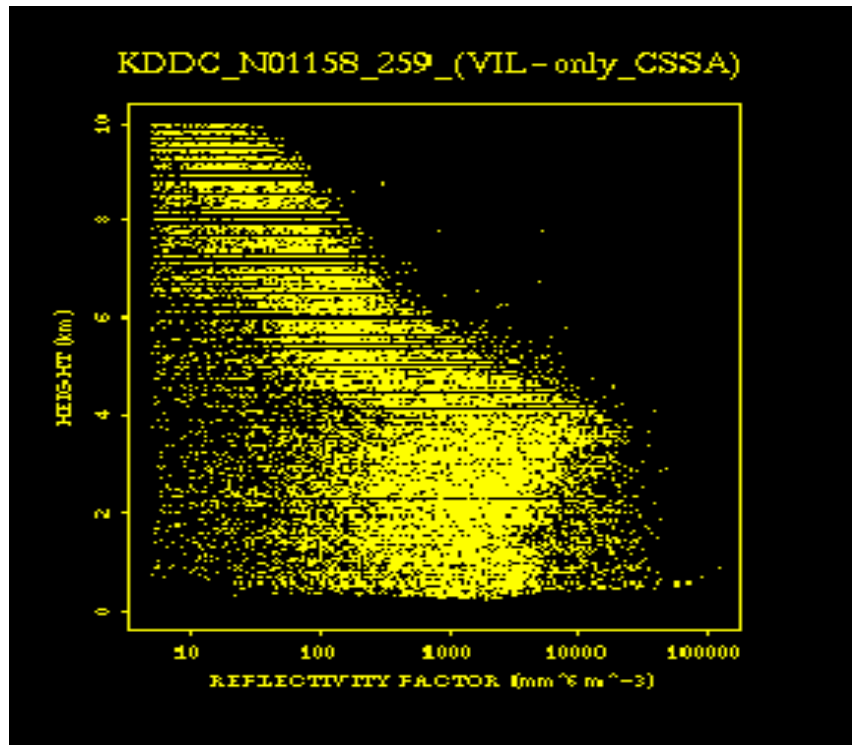


Figure 14. As in Fig. 13, except plot for KDDC (Dodge City KS) 14 July 1993.

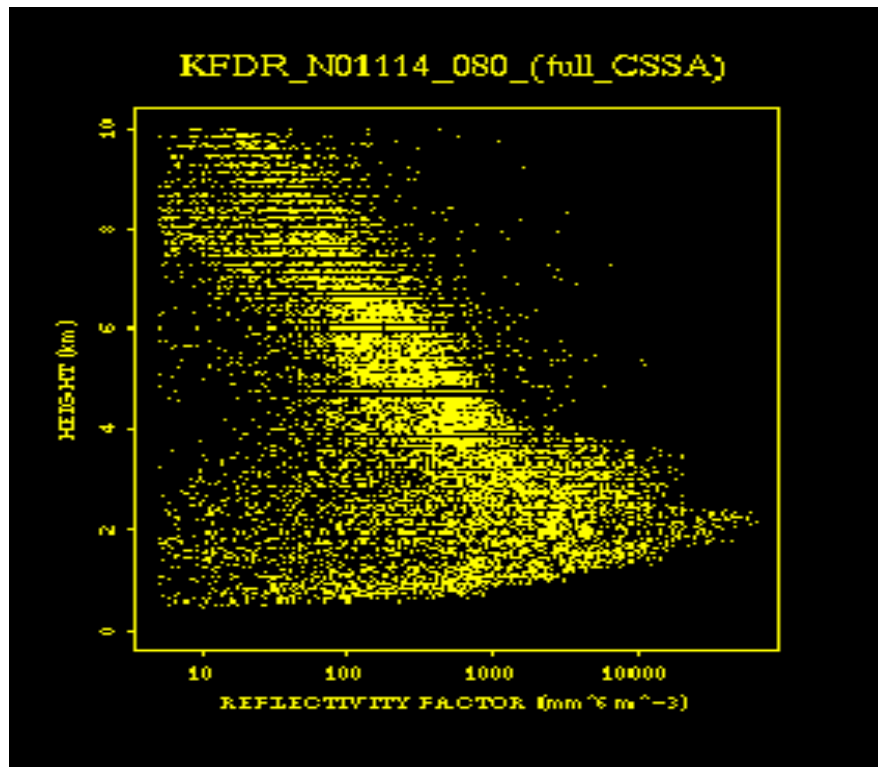
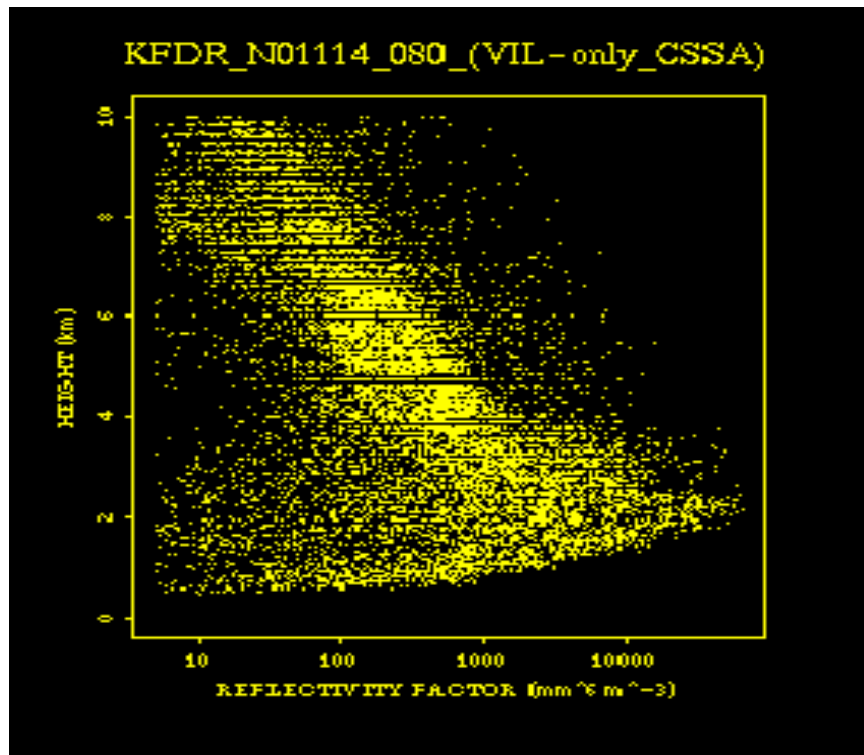


Figure 15. As in Fig. 13, except plot for KFDR (Frederick OK), 9 May 1993.

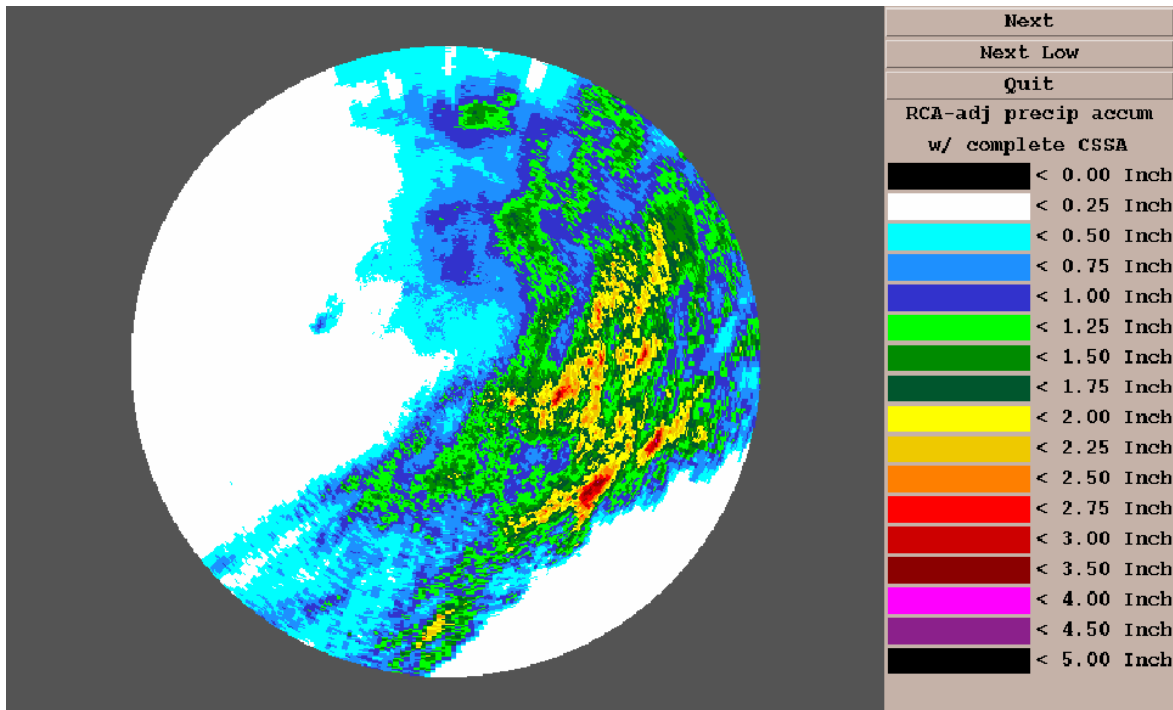
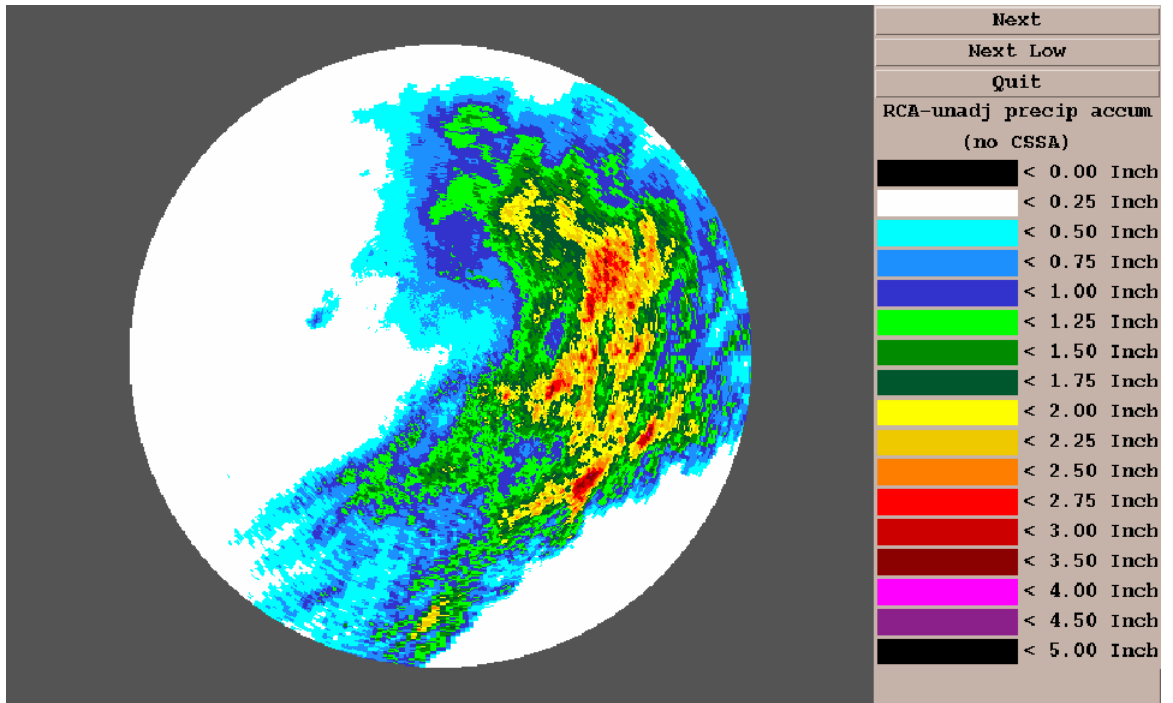


Figure 16. Precipitation accumulations (top) without and (bottom) with range correction and CSSA for KDDC, Jul 14, 1993

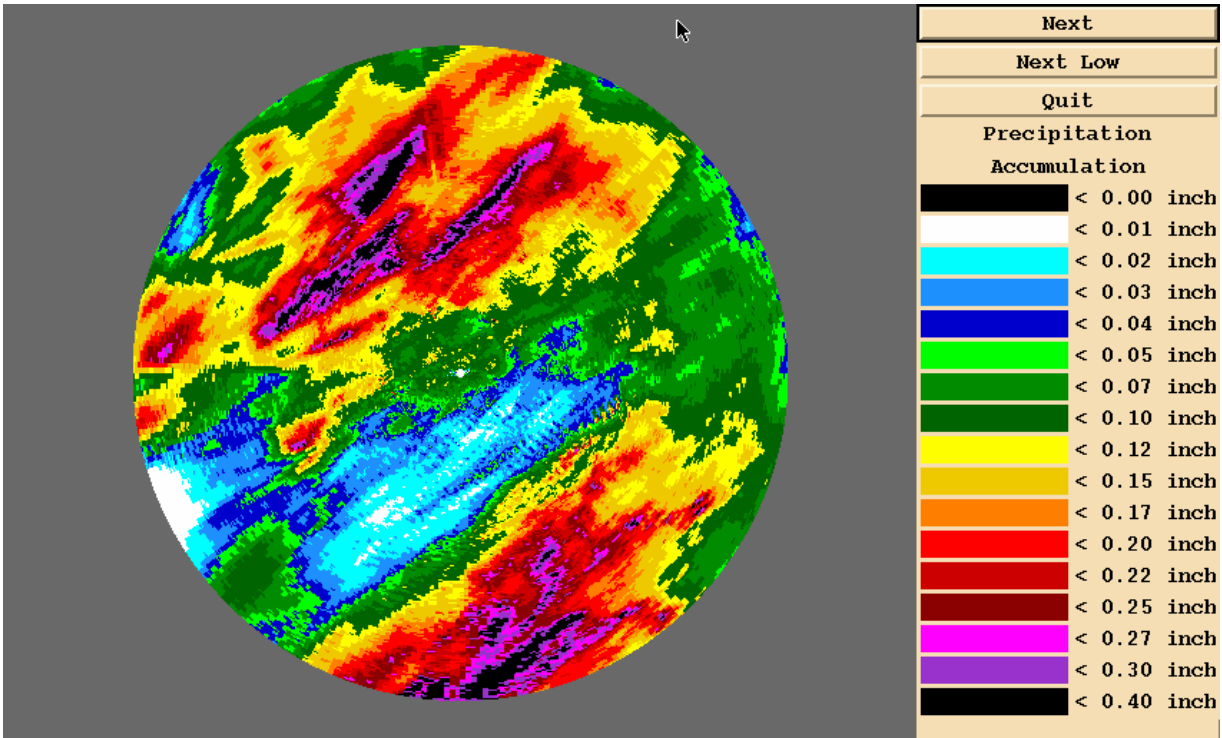
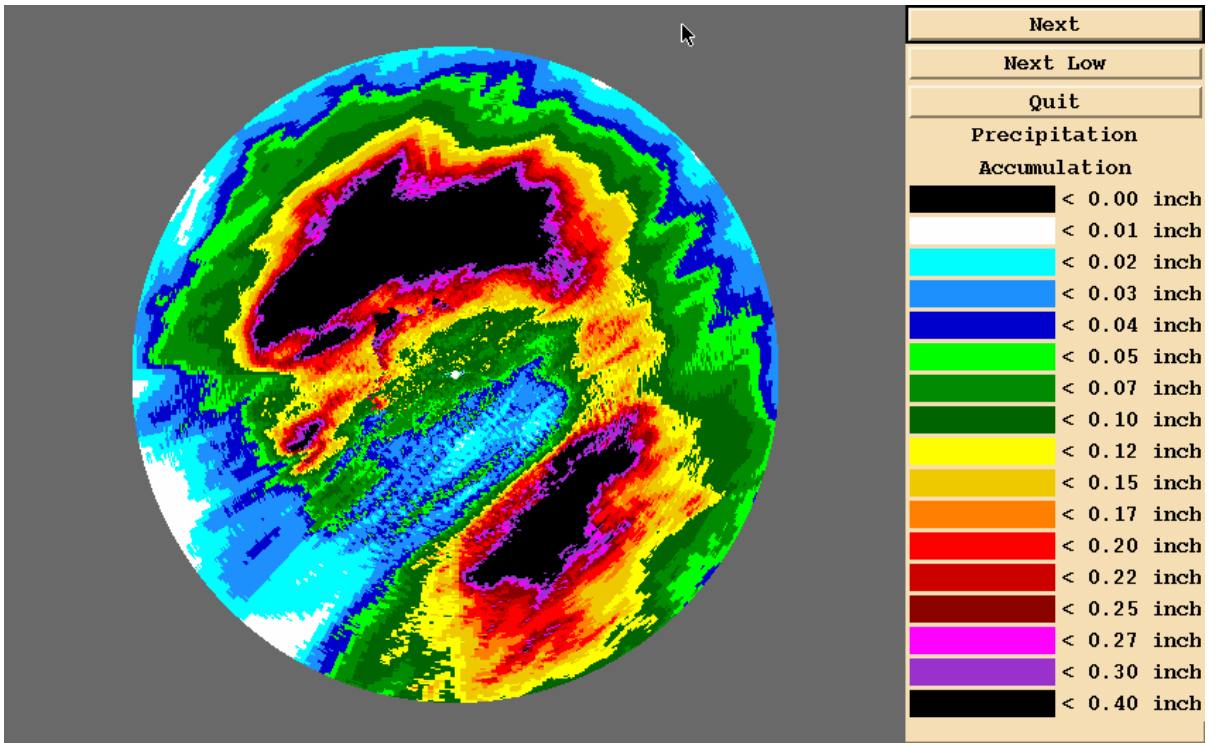


Figure 17. Precipitation accumulations (top) without and (bottom) with range correction and CSSA for KTLX, Jan 5, 2002

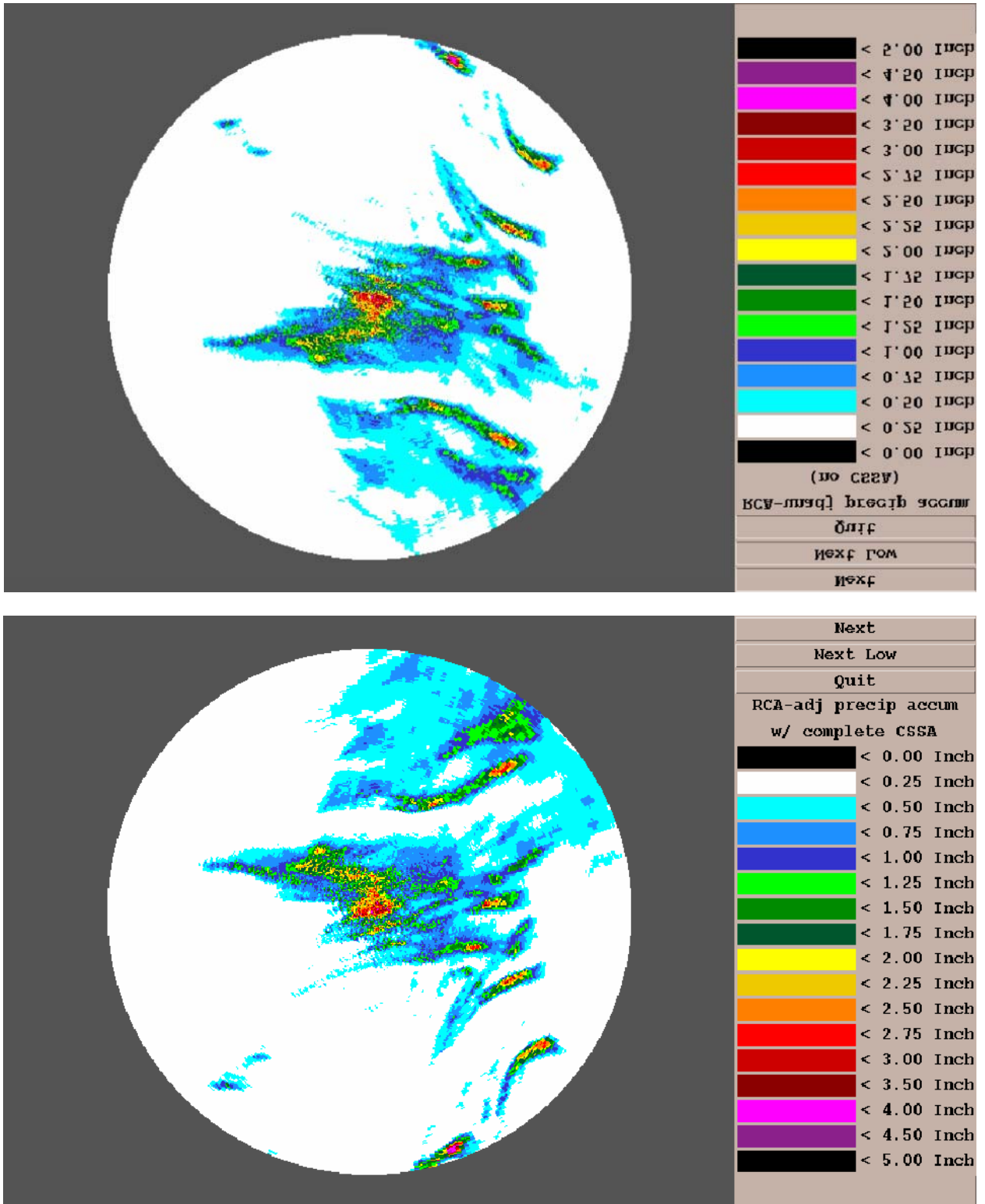


Figure 18. Precipitation accumulations (top) without and (bottom) with range correction and CSSA for KMLB, Mar 25, 1992

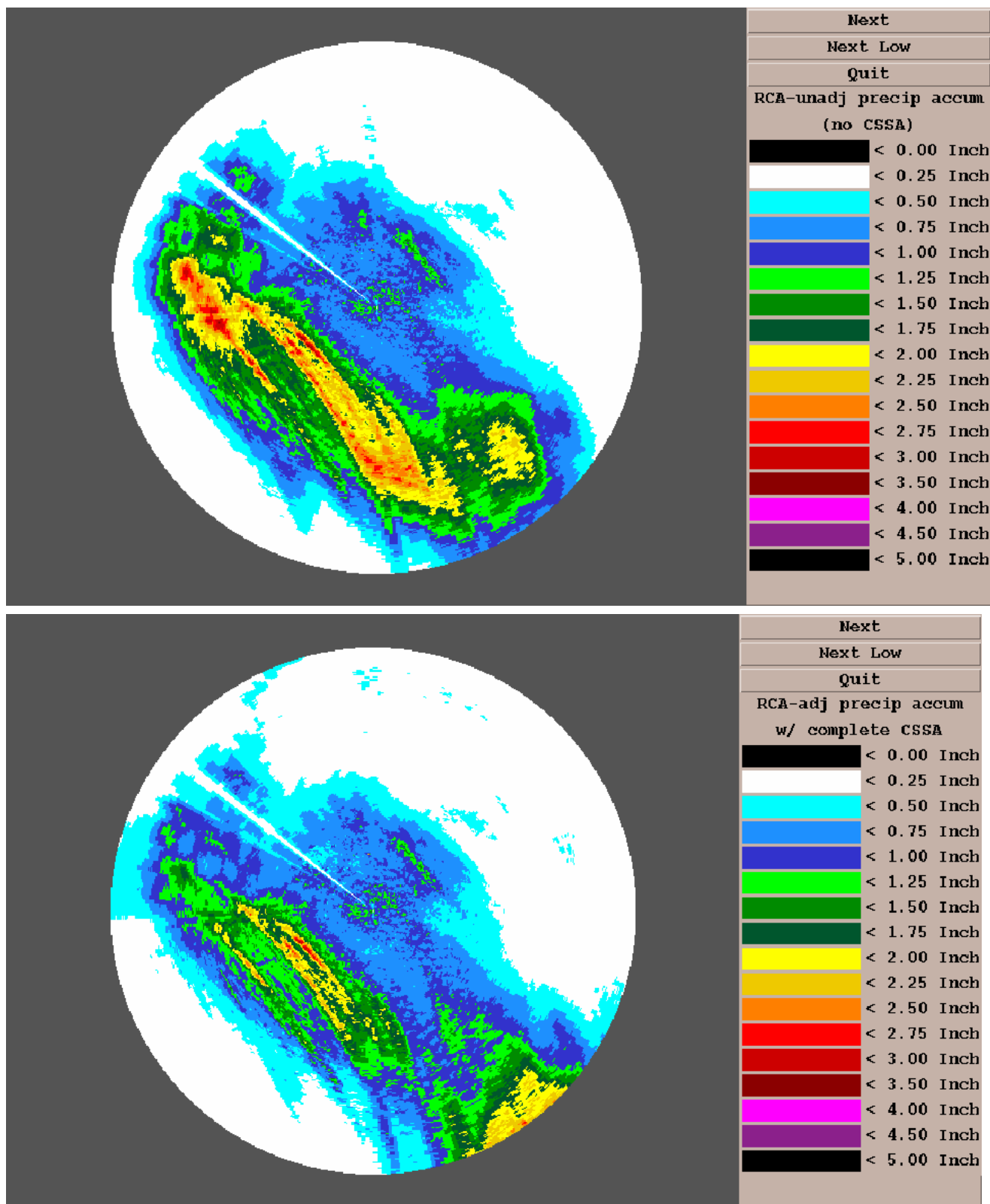


Figure 19. Precipitation accumulations (top) without and (bottom) with range correction and CSSA for KOKX, Oct 19, 1996

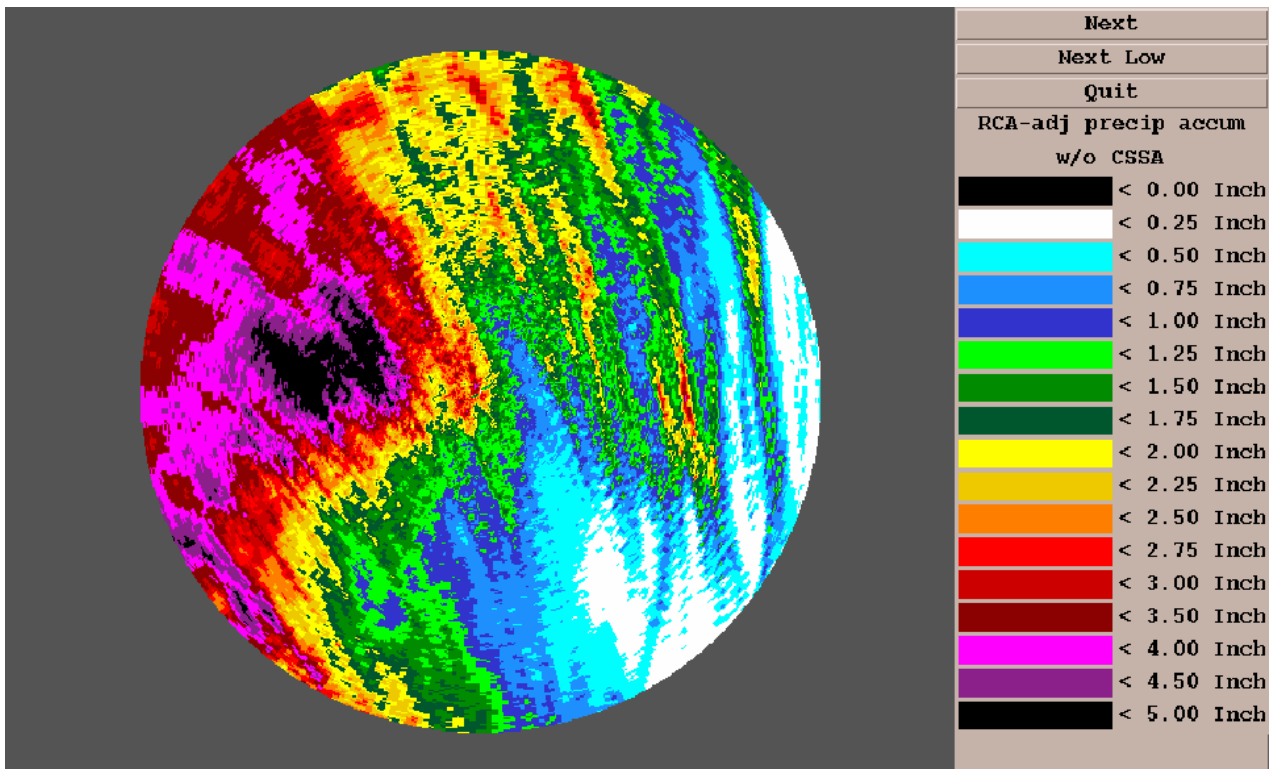
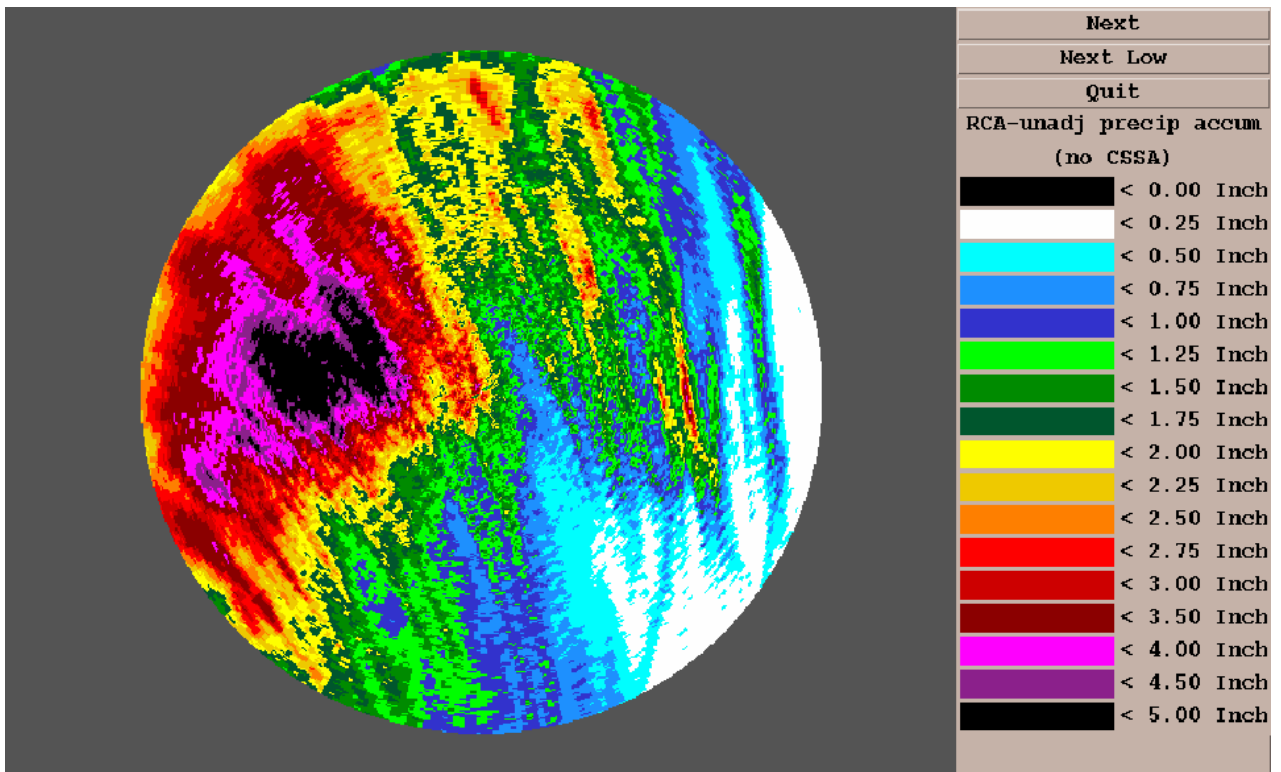


Figure 20. Precipitation accumulations during passage of Tropical Storm Opal, (top) without and (bottom) with range correction. CSSA was not applied. KEVX, Oct 4, 1995

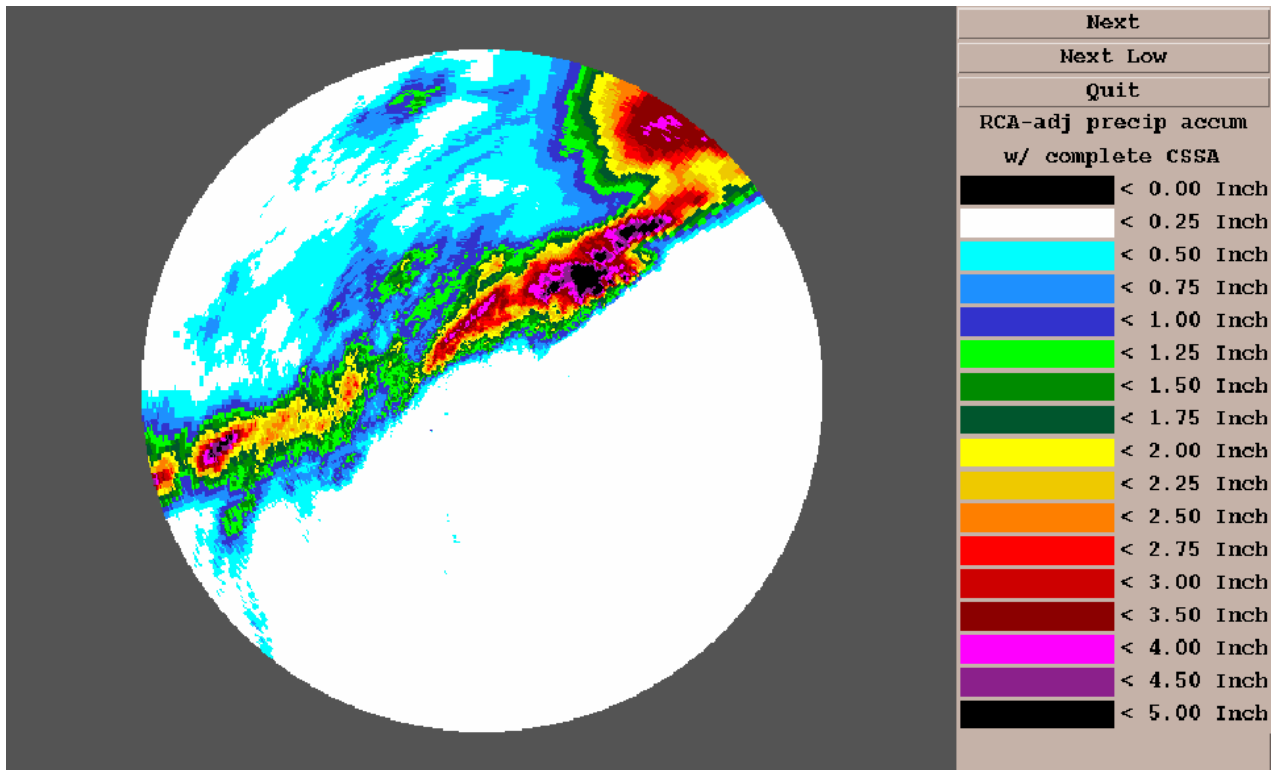
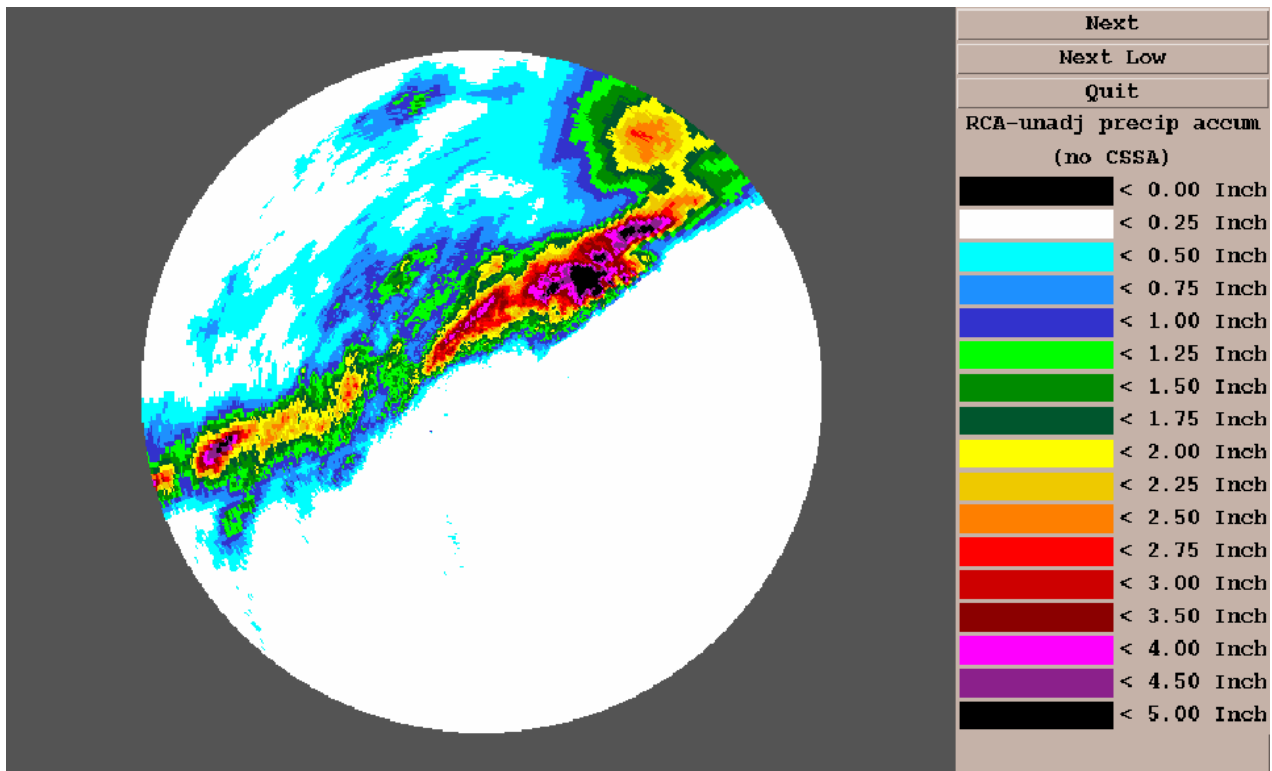


Figure 21. Precipitation estimates (top) without and (bottom) with range correction and CSSA for KHXG, Oct 17, 1994

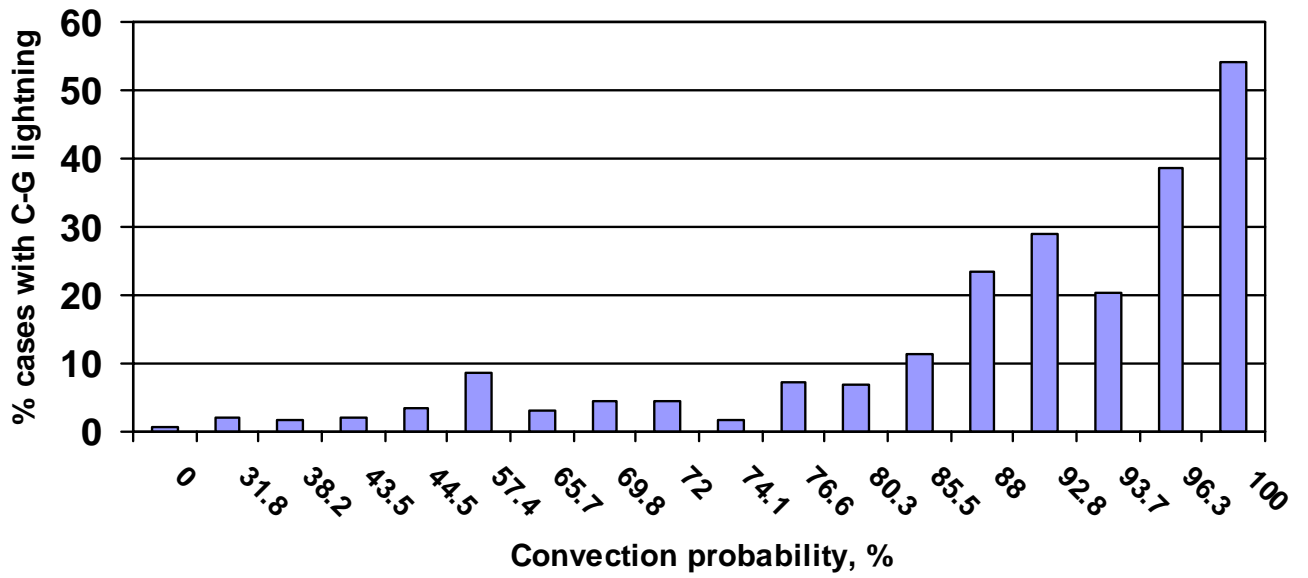


Figure 22. Percentage of 4-km grid boxes within radar umbrella with cloud-to-ground lightning as a function of convection probability. Total 104,000 cases with radar reflectivity  $\geq 5$  dBZ, from KRTX, KTLX, KPBZ, KRLX sites, April-May 2004.